

SINCRYS

A single-crystal diffraction
beamline at MAX IV

Detailed Design Report 2.0

Lennard Krause

Martin Roelsgaard

Peter Sondhauss

Mads Ry Jørgensen

August 10, 2023100723

Contents

1	Introduction	2
2	Beamline Design & Optics	5
2.1	Insertion Device & Front End	7
2.1.1	SINCRYs operation range	8
2.1.2	DanMAX IVU and monochromator statistics	9
2.2	Beamsplitter for beam multiplexing	10
2.3	Second monochromator crystal	12
2.4	Beam focusing	15
2.5	Heat load management	20
2.6	Vacuum system	22
2.7	Mechanical translations & specification	24
2.7.1	Crystal monochromator 1	24
2.7.2	Crystal monochromator 2	25
2.7.3	Transfocator	26
2.8	Beam diagnostic and shutter modules	27
2.9	Radiation safety	27
2.10	Effect of beamsplitter on transmitted beam to DanMAX	29
2.10.1	Absorption in high-pass filters	29
3	Experimental Hutch	31
3.1	Receiving beampipe and beam conditioning unit	31
3.1.1	Fast shutter	32
3.1.2	Attenuators	32
3.1.3	Slit systems	33
3.1.4	Beam intensity monitor	33
3.2	Goniometer	33
3.3	Detector	35
3.4	Detector positioning system	38
3.5	Automation and Sample Handling	40
3.6	Hutches and Infrastructure	41
4	Scandinavian Crystallography Service	42
5	Project Timeline & Budget	43
5.1	Budget	43
5.2	Installation considerations	43
A	Appendix A	50
A.1	Science cases and SINCRYs Consortium	50
A.2	Supporting information and illustrations	54
A.3	List of Abbreviations	57
A.4	Review report	58
B	Appendix B	58
B.1	MASH report	58

1 Introduction

Our modern civilisation is built using a wealth of materials, e.g.: metal alloys, semiconductors, pharmaceuticals, ceramics, polymers, etc. Throughout history our use and understanding of materials have evolved and allowed us to develop technologies that have transformed all aspects of our lives. Today, this field of science is known as materials science. In this field researchers study how the structure of a material gives rise to its properties and performance, and how these are affected by the synthesis and processing methods. In other words, a thorough understanding of the atomic structure of a material is fundamental to our understanding of its properties, and thus an essential step in our continued development of new advanced material. Exploration of new materials is indispensable e.g., for attaining sustainability, and continuous materials development is essential for maintaining a competitive Scandinavian industry.

Single-crystal X-ray diffraction (SCXRD) is the preferred technique to solve the atomic structure of a crystalline material. It is now a routine technique in many research laboratories, however, the limited flux, spectral purity and focusing ability of a lab-source severely limits the size and quality of the crystals that can be measured. Moreover, many materials do not grow crystals that are large enough to be studied by this technique. Modern synchrotron X-ray radiation sources can close this gap; however, they are not commonly used for routine small molecule crystallography due to the additional technical expertise required and long lead times in the proposal-based access policy. MAX IV is a world-class synchrotron X-ray source located in Lund, Sweden. MAX IV was the worlds first synchrotron to apply a multi-bend achromat lattice design leading to exceptionally small source sizes and source emittance, thus enabling unprecedented focusing options at the experimental endstations. There is, however, a gap in the experimental capabilities of existing - and in-construction - beamlines at MAX IV, namely the molecular single-crystals with small-unit cells and/or heavy elements (high Z). The existing macro-molecular crystallography (MX) and micro-focus beamlines are highly optimized for crystals that typically exhibit limited scattering power, show large unit cells and are generally compounds that are highly sensitive to radiation damage. They are specialized on a high throughput and therefore require an optimal but less flexible experimental setup which is less suited for small-molecular compounds.

DanMAX (<https://www.maxiv.lu.se/beamlines-accelerators/beamlines/danmax/>) is a multipurpose beamline for materials science dedicated to *in situ* and *operando* experiments on real materials under real conditions. The experimental suite covers a multitude of experiments with a wide span of energy from 15.0 – 35.0 keV, capitalizing on strengths within the Danish materials science community.

DanMAX had 'first light' in the fall of 2020 into its large experimental hutch (EH) that will eventually house 3 different experimental stations. The focus is on *in situ* powder X-ray diffraction (PXRD) experiments (in operation), full-field imaging (undergoing commissioning) and a high-resolution powder diffraction station (in procurement). DanMAX was built with a secondary hutch in mind, allowing a potential instrument upgrade towards a future sidestation with minimal investment, as the major infrastructure is already in place (source, experimental hutches and its infrastructure, see Figure 1).¹ The design report for DanMAX outlined such a vision by a clever exploitation of the existing high-pass filters in the optical path of DanMAX to allow hosting of a horizontally offset second train of optics, extracting and diverting a fraction of the white X-ray beam of the DanMAX in-vacuum undulator (IVU) into a second

experimental hutch.

This report develops this idea, and with some key changes to the optical concept, demonstrates the possibility of establishing a world-class single-crystal instrument that fills the currently underrepresented role of small-molecule single-crystal X-ray diffraction at MAX IV. It is funded by Nationalt Udvalg for Forskningsinfrastruktur (NUFI) under the Ministry of Higher Education and Science in Denmark. SINCRYST (<https://www.maxiv.lu.se/beamlines-accelerators/beamlines/danmax/experimental-station/sincrisys/>) is headed by Aarhus University and the project is carried out in collaboration with MAX IV (Lund University).

The purpose of the instrument to acquire high resolution 3D atomic structure data of crystals with dimensions of just a few micrometres. Due to the fundamental nature of the derived structural information, the instrument will serve an extremely broad research community in academia as well as industry and spans from bioscience and pharmaceutical sciences across chemistry, materials and geoscience to solid state physics. The instrument will expand the existing single-crystal techniques available at MAX IV. SINCRYST will be tailored for smaller unit cells commonly found in organic molecular crystals, inorganic materials and hybrid organic-inorganic compounds.

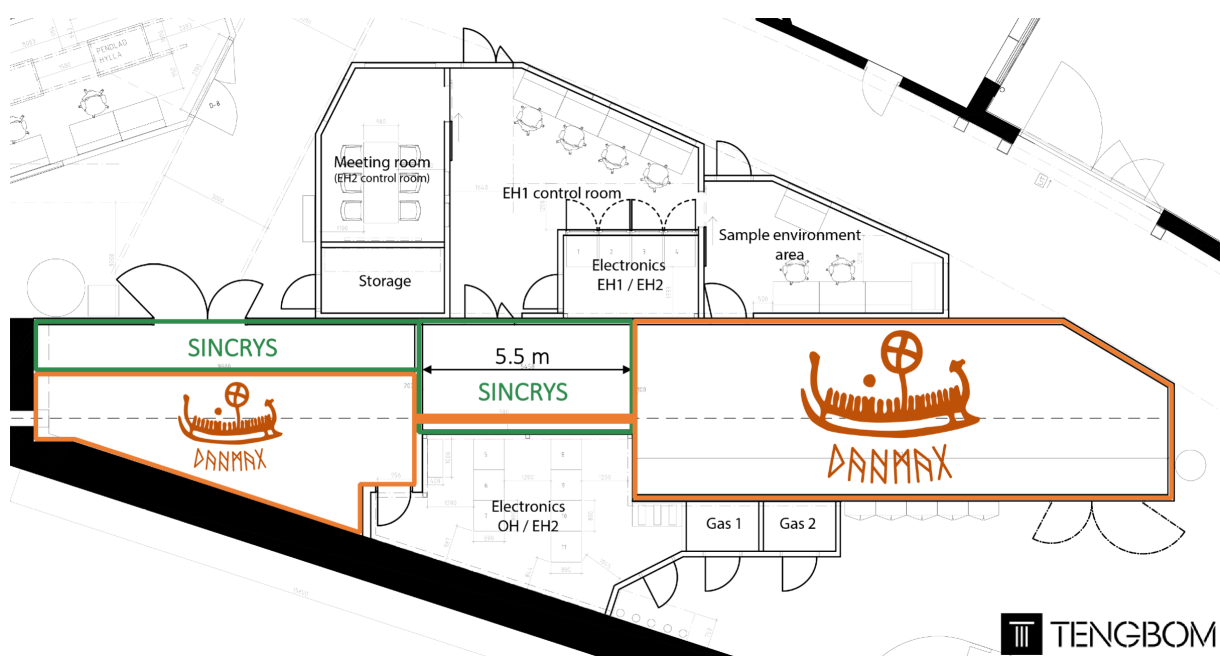


Figure 1: Floorplan showing SINCRYST (green) at DanMAX (orange).

A road map is outlined for the procurement and implementation of the SINCRYST sidestation. The report also envisions the benefit of establishing a Scandinavian Crystallography Service as a one-stop-shop to the benefit of the Scandinavian crystallographic community, by exploiting the highly automatized, high throughput nature of SINCRYST.

TDR 2.0

The first version of this design report (March 31st, 2023) was reviewed in April 2023. The external panel members consisted of Raymond Barret (ESRF) and Horst Schulte-Schrepping (DESY). A section adding a simulation of the wavefront propagation through a Bragg-crystal and exchanging Be compound refractive lenses have also been added to the raytracing report (see Appendix B) for a more detailed picture. The full review report is attached in Appendix B. The DanMAX and SINCRYS teams are grateful for the review and the this updated report reflects the suggestions made during the review.

During the review no design flaws or show-stoppers were identified. However, the review panel recommended the timely procurement of the optical solution presented in this report. Especially the transfocator and beryllium compound refractive lenses has been identified as a larger risk, for which the procurement should be advanced. Alternatives such as single-crystal diamond lenses should be investigated as an alternative. Supplementary ray tracing simulations show a reduced number of lenses required with a minimal reduced flux rendering them an attractive solution. The presentation of the design to the DanMAX steering group revealed a strong need to test and establish diamond CRL at MAX IV with regard to possible future upgrades of the optics of existing beamlines (e.g. DanMAX). Time has shown that flexibility towards future changes in application and adaptation to new fields and techniques is essential for long-term operability of the instruments. For SINCRYS, requiring only half the number of lenses when using C* enables us to leave certain cassettes of the transfocator empty, keeping it ready for future adaptations, while keeping the dimensions small.

For both of the monochromators, the panel recommended the use of thin HPHT 111 diamond crystal plates in Bragg geometry, and strongly argued against CVD diamonds (substantial flux losses due to poly-crystallinity) or a Laue configuration (larger aberrations and consequently a larger focal spot size).

2 Beamlime Design & Optics

In the early design phases of the DanMAX project, several options were discussed to house the individual techniques in separated and independent end-stations, one focusing on full-field imaging and another one on powder X-ray diffraction. However, it was quickly realized in the technical design phase, multiplexing the beam and working with two separate branches was not a feasible pathway. The major concern was that both techniques eventually would want access to the full energy spectrum of the undulator source and it was therefore considered unreasonable that both sections would be operating simultaneously most of the time. Spending an unreasonable amount of time on setup and adjustment would diminish the advantage of having two beamlines in parallel.

A second experimental hutch (EH) was built to allow future multiplexing of the DanMAX beam, by extracting a monochromatic beam from the white beam with a crystal beamsplitter (BS).¹ This second, monochromatic beam is guided into a secondary hutch (EH2) that can operate simultaneously and independently of the main branch. The necessary investment into a multiplexing solution is thus far lower than a complete beamline budget. The X-ray source and all front-end (FE) optics are shared leaving minimal impact to the main branch. However, under the condition that a sufficiently transparent beamsplitter for the multiplexing is picked to ensure no effect on flux and beam quality of the main branch. The original proposal was based on using a thin Diamond crystal (C^*) Laue plate as beamsplitter diffracting off the (111) set of planes and extract a fraction of the 5th or 7th undulator harmonic. A Germanium crystal Ge(220) was envisioned as a second monochromator crystal acting to parallelize the beam after a horizontal offset to guide the monochromatic second beam into EH2. The proposed concept is schematized in Figure 2, and will be detailed in the following chapter.

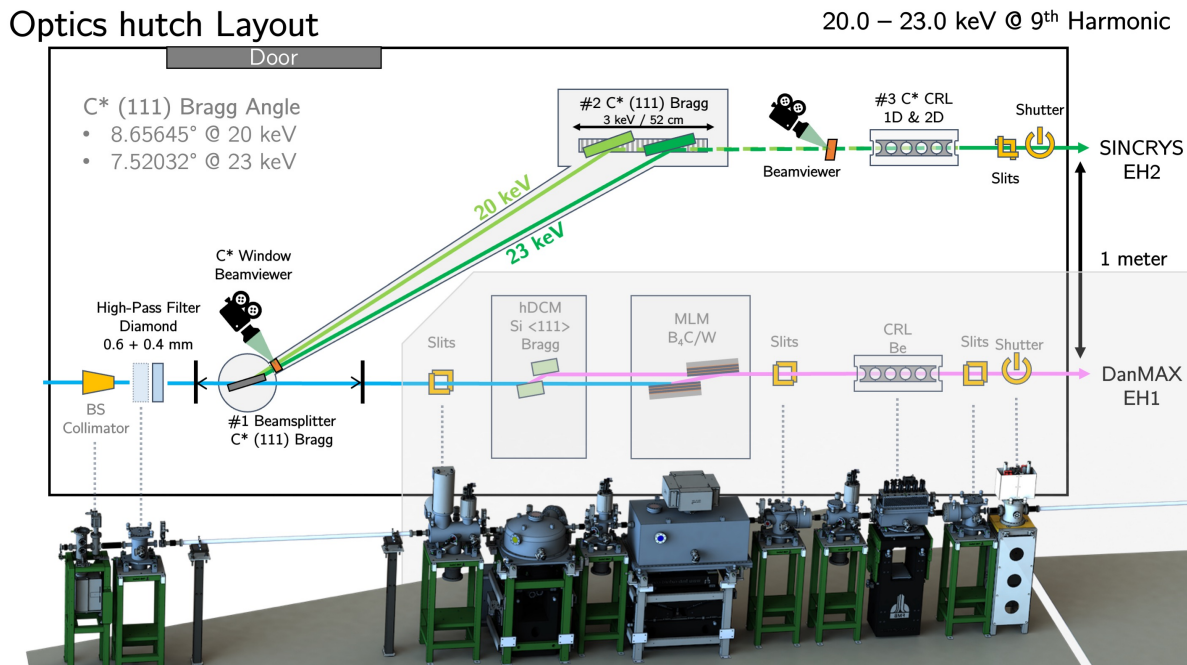


Figure 2: Sketch of the optical setup for SINCRYST. A beamsplitter is positioned within the DanMAX white beam section, and extracts a span of 20.00 – 23.00 keV towards SINCRYST.

There are some key differences to the original concept, namely using photon energies centered primarily on the 9th harmonic (20 – 23 keV), and two Bragg-configured diamond monochromator crystals, in place of the Ge(220) monochromator.

Ray-tracing simulations and finite element analysis (FEA) have been performed in MASH (Macros for the Automation of Shadow).² MASH is a tool to automate Shadow, including heat load calculations with FEA, so that the user only needs to provide the optical setup for evaluation. The results are worked into the relevant sections below, and the detailed simulations from the FEA and ray-tracing analysis can be found in Appendix B.

A right-handed coordinate system is employed throughout this document, as schematized in Figure 3. The thumb of a right hand corresponds to the positive horizontal X direction, the index finger to the positive vertical Y direction pointing upwards, and the middle finger (positive Z) to the direction of the photon beam. For the global coordinate system, the positive Z axis is along the photon beam from the insertion device (ID).

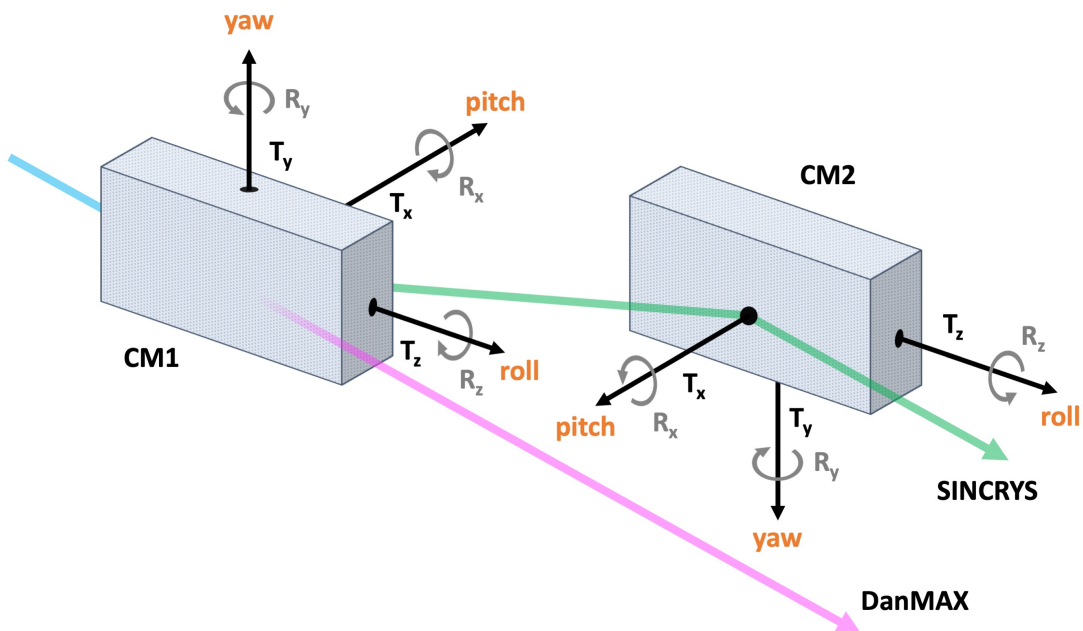


Figure 3: Coordinate system used in this report. Z is oriented along the beam direction (downstream), positive Y is pointing against gravity and positive X is pointing outbound. Yaw is tuning the Bragg angle.

2.1 Insertion Device & Front End

The existing DanMAX insertion device is only briefly presented. A detailed discussion can be found in the DanMAX design report.¹ It was opted for a permanent magnet in-vacuum undulator by Hitachi Metals Ltd., as this optimizes a maximal photon flux at the highest operation energy of 35 keV photon energies. The IVU is installed at achromat 4 at the 3 GeV ring at MAX IV. The IVU and part of the front-end is depicted in the photograph in Figure 4, and key parameters are listed in Table 1. The magnetic period length is 16 mm with 187 periods for a full length of approximately 3 meters (using the maximal length of the section incl. essential infrastructure at each end of the section), with a minimal gap of 4 mm.

Table 1: DanMAX undulator parameters. The source size and divergence is $53.9 \times 6.4 \mu\text{m}^2$ and $11.3 \times 9.8 \mu\text{rad}^2$, respectively (H×V RMS).

DanMAX 3 m IVU16		
Period length	[mm]	16
Periods	[#]	187
Magnetic Gap range	[mm]	4.0 – 50.0
Peak field	[T]	1.181
Effective peak field	[T]	1.114
Effective K_{max}		1.66
Magnetic pole material		NdFeB
Pole material		Vanadium Permendur

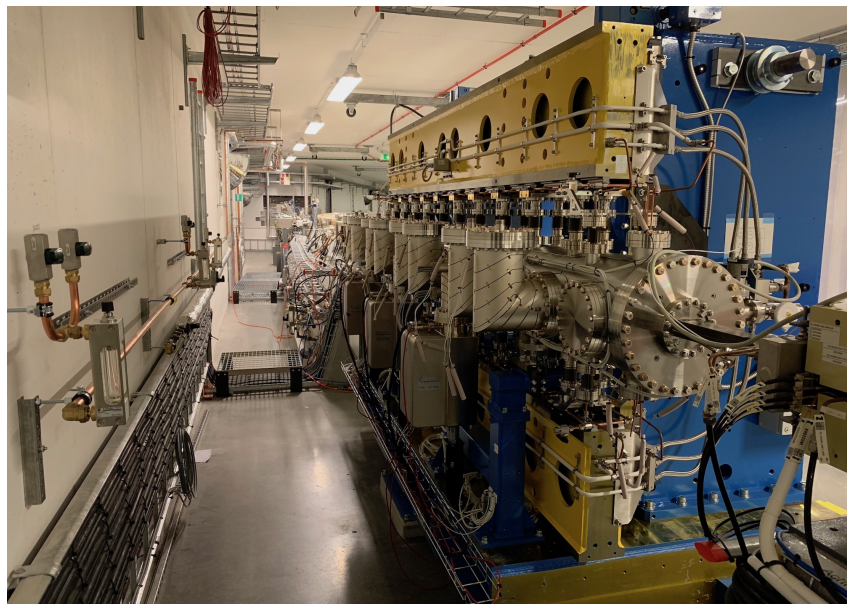


Figure 4: The DanMAX IVU16 installed at the 3 GeV ring at MAX IV on the 4th achromat section.

The DanMAX FE was built and installed by Toyama, and is designed to protect users and equipment from radiation, as well as for vacuum failures. SINCRYST will make no modifications to or have any impact on the FE. It is only mentioned here briefly as it defines relevant beam parameters that are discussed in the following sections. In the FE a number of both movable and fixed masks limits the transmitted power downstream of the FE, by defining the transmitted beam. It is defined by an acceptance cone in the FE at $35 \times 35 \mu\text{rad}^2$ matching the extent of the central cone of the ID. The maximum transmitted power through this aperture is 125 W.¹ This acceptance limit is implemented in the beamline programmable logic controller (PLC) system to ensure the beam shape defining aperture masks positions can be scanned, however, not exceed the limits.

2.1.1 SINCRYST operation range

DanMAX offers the photon energy range 15 – 35 keV by adjusting the magnetic gap distance to fine-tune the magnetic field exerted on the electrons in the storage ring. This adjusts the ID output to the desired energy. To pick a certain undulator setting, the gap between the magnets of the source is adjusted within an operation range of 4.4 – 50.0 mm, to achieve an effective field of 1.114 T at the minimal gap. The spectrum from an undulator ID consists of a set of narrow high-intensity peaks that are equally spaced in energy, approx. 2.4 keV apart. The span of distances have been simulated in SPECTRA³ and is available from the DanMAX optics web page ([https://www.maxiv.lu.se/beamlines-accelerators/beamlines/danmax/beam line-optics/](https://www.maxiv.lu.se/beamlines-accelerators/beamlines/danmax/beam-line-optics/)).

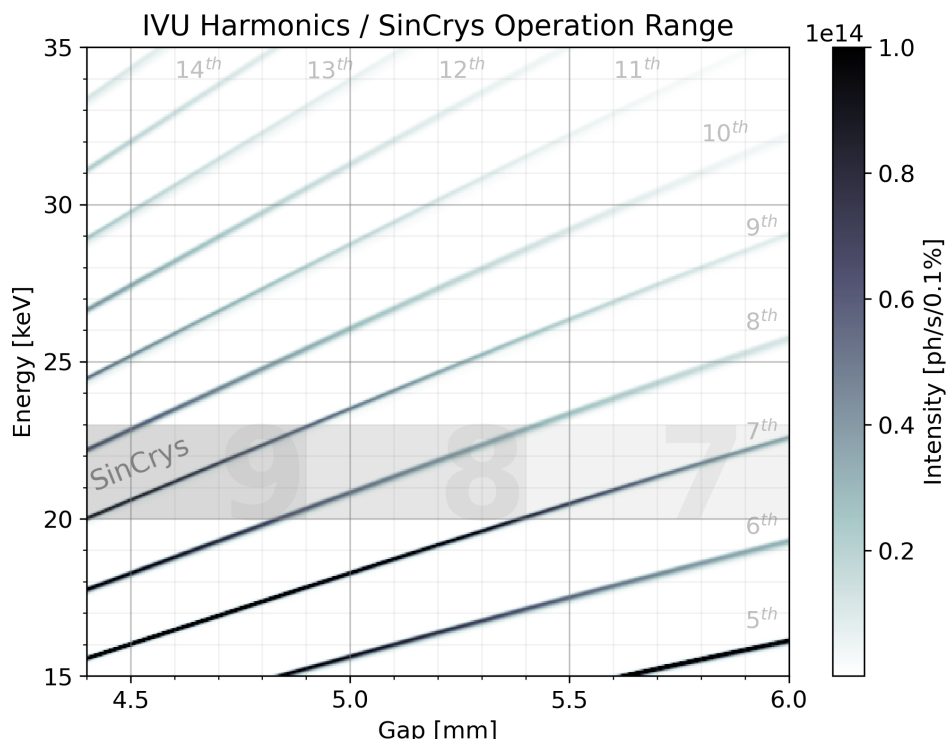


Figure 5: Heat map of the photon flux of the DanMAX IVU16 as a function of gap distance and photon energy. In gray: Operation range for the SINCRYST side station at different IVU harmonics between 20.0 and 23.0 keV.

The 7th harmonic with an energy close to 17 keV is reserved for the imaging instrument that is currently in the procurement phase at DanMAX, which will be commissioned during 2023. The imaging instrument will utilize a broader part of this undulator peak as it covers an energy range well suited for most imaging experiments. It would be unfavourable to cut out a small fraction of the harmonic peak, causing a dip in the spectrum, impacting the normal operation considerably. The next natural choice for SINCRYS falls to the 9th harmonic, ranging approximately from 20 to 23.0 keV in photon energy over the undulator gap range.

The heat map in Figure 5 shows the photon flux as a function of energy and gap distance for all gap distances between 4.4 to 8.0 mm. The greyed areas thus indicate the harmonic SINCRYS will operate with for any given gap setting of the IVU. For large gap values above 5.0 mm it may be necessary to switch and use the 8th or even 7th harmonic, at the cost of photon flux. As already mentioned, the 7th harmonic is considered to be reserved for the imaging instrument. However, there will be no conflicting situation as it is unlikely that the imaging instrument would open the gap to operate using the 7th harmonic as smaller gap values would increase the flux. With a fundamental photon energy of 2.24 keV for DanMAX, λ_9 corresponds to 20.16 keV with a minimal gap of 4.0 mm. The SINCRYS energy range thus spans from 20.00 – 23.00 keV. This is a necessary consideration as the energy SINCRYS will operate with is determined by the IVU gap set by DanMAX. In the current scheme DanMAX will attempt to schedule and cluster experiments that can use 'any' energy to facilitate SINCRYS operation. Experiments that require exact gap values force SINCRYS to continuously tune to new energies which might turn out to be unfeasible and it is currently anticipated that the side branch remains nonoperational for the duration of such experiments.

2.1.2 DanMAX IVU and monochromator statistics

The DanMAX beamline control software stores the undulator gap distance (and other metadata) for each performed scan. It is straightforward to extract all the gap distances and make a histogram of the most frequently used values to determine the general range of application. However, it should be noted that the distribution is subject to change with the imaging instrument entering operation. A histogram of the use case parameters is presented in Figure 6. The trawl through all metadata resulted in an (in practice) operational undulator gap range between 4.4 – 5.7 mm for all experiments performed at DanMAX excluding test-scans without X-ray flux in the EH (and inconsistencies in the scans where the appropriate metadata was not saved, accounting for approx. 50 % of the scans, in particular in the early commissioning). It is evident that the DanMAX users thus far have operated with gaps that would allow SINCRYS operate on the 9th harmonic approximately 75 – 80 % of the time.

The 7th harmonic has a maximal flux output at 17.0 keV at a gap value of 4.716 mm, likely presenting no issues for SINCRYS to use the 9th harmonic, while DanMAX is operating in imaging mode. Furthermore, at high gap-values, there is the possibility of harmonic-hopping and to select the 8th or 7th harmonic in the interval of 20.0 – 23.0 keV, although at the cost of a reduced photon flux.

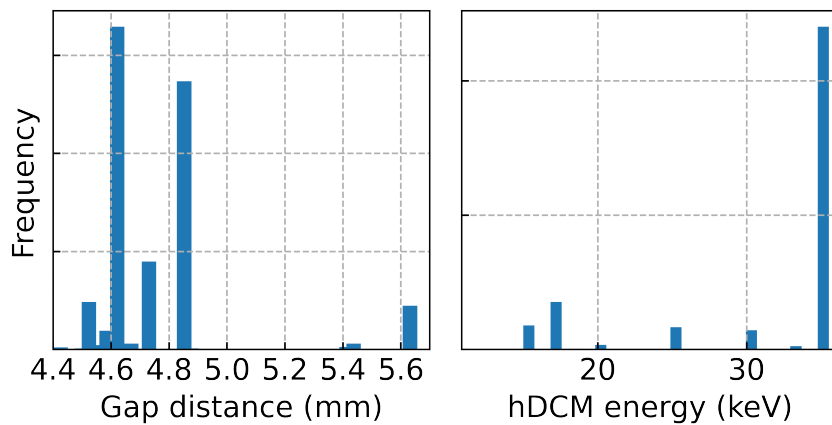


Figure 6: Typical IVU gap values and target hDCM energies. Data collected on 08.12.2022 from general beamline operation metadata.

2.2 Beamsplitter for beam multiplexing

The concept of multiplexing an X-ray beam with a crystal monochromator was pioneered in 1994 by Als-Nielsen *et al.* at the TROIKA end-station at the European Synchrotron Radiation Facility (ESRF).⁴ To effectively multiplex an X-ray source, a sufficiently X-ray transparent crystal is required *i.e.* a thin crystal with a long photo-absorption length. The extinction length (*i.e.* the Bragg reflectivity) is ideally shorter than the photo absorption length to maximize the flux in the scattered beam. A small collection of instruments that employ (or employed) beamsplitters are summarized in Table 2.

Table 2: Summary of other beamlines employing diamond crystals as beam splitting elements.

Beamline	Material & refl.	Reference
CHEX	C* (111), (220), (400)	APS-U ⁵
LCLS	C* (111)	Zhu <i>et al.</i> ^{6,7}
MASSIF-1	C* (110)	Bowler <i>et al.</i> ^{8,9}
P02.1	C* (111)	Dippel <i>et al.</i> ¹⁰
Cassiopeia	C* (111)	Ursby <i>et al.</i> ¹¹
Hyogo	C* (220), (400)	Tsusaka <i>et al.</i> ¹²
Troika	C* (111)	Als-Nielsen <i>et al.</i> ⁴

The most common beamsplitter choice are high-purity, synthetic type IIa diamonds, grown with a high-pressure, high-temperature (HPHT) technique, as they are generally considered to have the highest crystal quality and the lowest density of defects. Diamond has an extinction length is about 1 % of the photo-absorption length, *i.e.* a diamond crystal can have a near-100 % Bragg reflectivity while absorbing only little of the incident white beam.¹³ The low photo-absorption and very high thermal conductivity of diamond also helps towards a simple cooling

scheme, in contrast to the necessary cryogenic cooling common for Si-based monochromators (incl. the DanMAX horizontal double-crystal monochromator, hDCM). The term beam splitter (BS) and 1st crystal monochromator (CM1) are used synonymous throughout this document and refer to the first optical element introduced by the SINCRYS station.

The type of crystal to employ is arguably the most critical question to answer and a rationale for the decision for a C*(111) in Bragg geometry is given in the following. For SINCRYS, the beam splitter must be chosen to maximize the diffraction efficiency while keeping a low absorption of the transmitted white beam and retaining the wavefront, to limit the effect on the DanMAX branch. The reflecting crystal and the reflection have to match with the geometrical constraints of the optics hutch, e.g. must provide a deflection angle to offset the beam by 1.0 m over a reasonable distance downstream. A larger deflecting angle is preferable as it lowers the spacing problem for following optical elements placed downstream.

Four different beam splitter solutions were considered for the design of SINCRYS, as summarized in Table 3. The discussion below will briefly mention cases #1 – 3, but the simulations are attached in Appendix B (Part I).

Table 3: Summary of candidates as first beam splitting monochromators (CM1) considered in the simulations for SINCRYS.

Case	Crystal	Reflection <i>hkl</i>	Geometry	Thickness [μm]
#1	Si	(111)	Laue	30
#2	Si	(333)	Laue	20
#3	C*	(111)	Laue	100
#4	C*	(111)	Bragg	100

Si(333) provides large deflection angles, $2\Theta_B \approx 32^\circ$, but compared to C*(111) or Si(111) five to eight times lower reflectivity and thus five to eight times less flux in the extracted, monochromatized beam, primarily due to its small structure factor. Silicon (111) on the other hand has a deflection angle of $2\Theta_B \approx 10.4^\circ$, and would need 5.54 metres between the beam splitter and 2nd crystal monochromator (CM2) to facilitate a horizontal offset of 1 meter.

As absorption is much higher in silicon, deformation under heat load is much larger if it is not kept at cryogenic temperatures. Deformation reduces reflectivity considerably. Hence, both silicon variants need cryo-cooling, by exploiting silicon's zero thermal expansion at 125 K.¹⁴ Otherwise, their reflectivity lags behind that of diamond and temperatures rise above 200 °C. Above that, the thickness of the silicon beam splitter has been chosen to be ambitiously thin, as to give them a chance despite of their considerably higher absorption. Whilst silicon wafers of 30 or 20 μm are not unheard of, the question remains, whether the crystal structure quality, the stability and longevity is sufficient for a monochromator. We are not aware of any monochromators with such thin crystals, and it would hence be highly experimental.

Using a C*(111) reflection, either in Laue or Bragg geometry, seems to be the best option. The flux in the monochromatic beam is comparable to that of cryo-cooled Si(111), and the deflection angle is with $2\Theta_B \approx 16^\circ$ considerably larger, allowing for a moderate 3.66 m between the crystals. In Bragg geometry, the thickness is not too critical, unless chosen unreasonably

thin, due to the relatively short extinction length in diffracting conditions. A thick crystal slab comes with a higher absorption of the beam that is passed to the DanMAX branch. A C* thickness of 100 μm has been used in this work.

Either Laue or Bragg geometry, both cases reflect off of the (111) plane as the (111) reflection of Diamond is strong and maximizes the photon flux in the diffracted beam. Synthetic diamonds are usually grown exposing the (100) face, so it has until recently been difficult to obtain high-quality crystals with a (111) face that has a area large enough for use as a crystal plate for symmetrical Bragg reflections. Sourcing that crystal is thus a concern in obtaining a high-quality C* with a (111) face, that is not helped by the lower incident angle in Bragg geometry compared to an asymmetric Laue reflection. More recently, however, synthetic crystals exposing the (111) faces have appeared commercially and in the literature.^{6,15,16}

2.3 Second monochromator crystal

The BS will deflect a monochromatic beam to the vacuum chamber of CM2. The distance between the first and second monochromator is given by $d = 1000 \text{ mm}/\sin(2\theta_B)$ behind the beamsplitter, with 1000 mm being the outboard horizontal offset to the white beam path, and θ_B the Bragg angle. The parallel length along the white beam path is given by $l = d \times \cos(2\theta_B)$. These distances are listed in Table 4 and sketched in Figure 7 for clarity. The resulting difference from 20 – 23 keV is 513.40 mm along the SINCRYS beam axis. The center of CM2 must traverse this distance on an axis parallel to the white beam axis.

Table 4: Distance between beamsplitter and CM2 at 20-23 keV photon energies. See also 7 for a sketch.

Energy [keV]	BS-CM2 distance d [mm]	Parallel to beam path l [mm]	Angle θ_B [°]
20.00	3360.33	3208.09	8.65645
20.30	3409.57	3259.63	8.52756
21.80	3656.06	3516.64	7.93688
23.00	3853.50	3721.49	7.52032

For the receiving monochromator, a germanium crystal with a (220) face was considered to quasi-parallelize the two photon beams again. Ge(220) has a Darwin width (DW) that is approximately a factor of 3 larger than C*(111) in the relevant energy range, see Figure 8. This would have had the benefit of making the alignment of the two monochromators straight forward and decrease sensitivity of the system to mechanical vibrations.

The d spacing of the Ge(220) reflection is only approximately 3 % smaller than C*(111), which would result in a minor deflection from a parallel line to the white beam axis of around 8.2 mrad. This creates an offset in the beam position at the sample position, a large fraction of which could be compensated by a lateral translation of the receiving crystal (CM2). The discrepancy in deflection angle also has an energy dependent part, as C* and Germanium differ in their dispersive properties. Over the given energy range this part varies over 0.6 mrad,

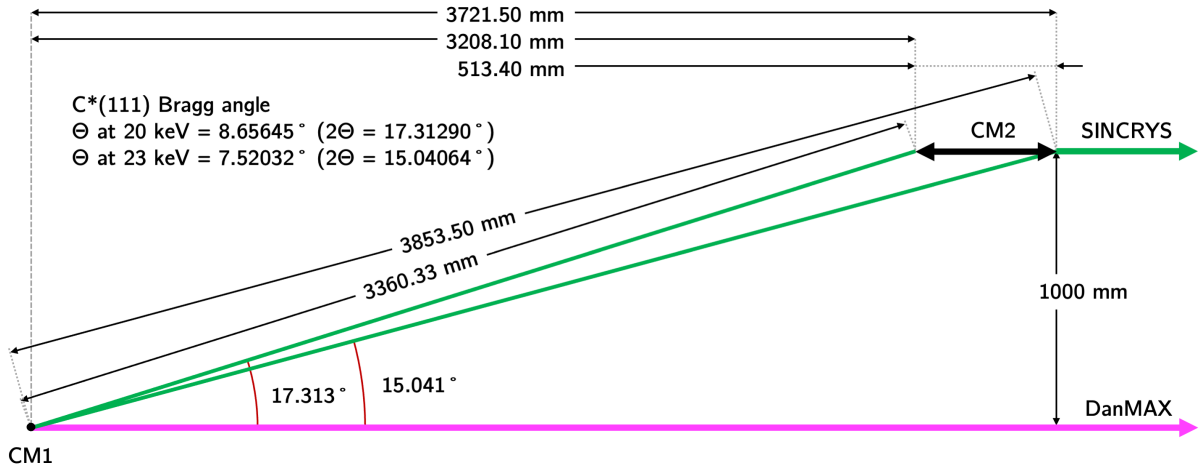


Figure 7: Sketch of the angles and distances between the two monochromator crystals.

visible in the difference of the Bragg angles given in Table 5. This is the effective offset all components downstream of CM2 would have to compensate.

Table 5: Bragg θ scattering angles for a C*(111) $d = 2.059408 \text{ \AA}$ and Ge(220) $d = 2.00033 \text{ \AA}$.

Energy [keV]	Diamond (111)		Ge(220)		Mismatch	
	[deg]	[mrad]	[deg]	[mrad]	[deg]	[mrad]
20.00	8.65645	151.084	8.91415	155.581	0.25770	4.498
20.30	8.52756	148.834	8.78136	153.264	0.25380	4.430
21.80	7.93688	138.525	8.17285	142.643	0.23597	4.118
23.00	7.52032	131.254	7.74375	135.154	0.22343	3.900

Over the distance of 1 m, the discrepancy in d spacing corresponds to a shift of the beam position in the order of a millimeter, considering only the dispersive part of the mismatch *i.e.* neglecting the static offset. This energy dependent offset is on the order of the entrance aperture of the compound refractive lenses (CRLs). The lateral position of the CRLs must therefore be adjusted, as well as all components downstream including the sample position. If one would use focusing mirrors instead, only the mirror angle would need to be tuned, which is probably why Ge(220) is a popular choice in combination with diamond beamsplitters at other beamlines.

In combination with CRLs, C*(111) as the second monochromator crystal avoids a lot of complications in the form of extra actuators, motion control units and a generally large number of degrees of freedom that need to be adjusted upon change of energy. Therefore, a C*(111) in Bragg geometry is preferable for both crystal monochromators.

One concern for this homogeneous combination of monochromators was the contamination of the beam by higher harmonics ($E_{Ph} \times 3$) as it would not offer any intrinsic suppression (*e.g.* the angular mismatch for the C*(111) + Ge(220) case). However, the ray-tracing simulations a

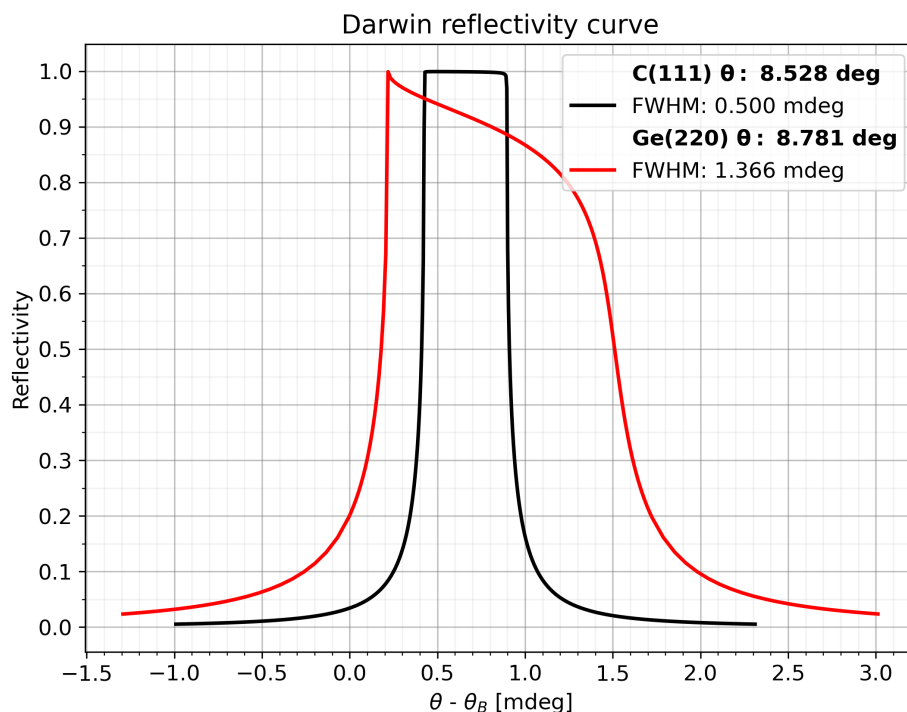


Figure 8: Overlay of the angular width of the reflectivity for $C^*(111)$ and $Ge(220)$ monochromators at 20.30 keV. The Darwin widths are 0.500 mdeg (8.94 μ rad) and 1.366 mdeg (23.82 μ rad), respectively.

minor beam contamination on the order of 10^{-5} for the $C^*(111)_{\text{Bragg}} + C^*(111)_{\text{Bragg}}$ scenario. In reality, it will most likely be even weaker. Indeed, for the $CM1_{\text{Laue}} + CM2_{\text{Bragg}}$ the high harmonic contamination is exceptionally low (in the order of 10^{-8}) or $C^*(111) + Ge(220)$ heterogeneous combinations.

Figure 9 shows that within the anticipated precision of the CM2 goniometer ($\approx 10 \mu$ deg), it should be feasible to detune the monochromator to avoid the higher harmonic contribution (see also Table 9). A detuning of just 1 μ rad thus further weakens the higher harmonic contamination by another 2 orders of magnitude, see Figure 30 (Appendix A). Moreover, the current stack of CRLs will focus the higher harmonic contribution less efficiently, thus decreasing the effective flux density at $3 \times E_{ph}$ significantly.

The thickness of CM2 is chosen to exceed the extinction depth to facilitate a reflectivity of close to 100 %. There is no transmitted part of the beam for CM2, and no upper limitation on the thickness. The DW of the $C^*(111)$ reflection is of course identical for the two crystals requiring their mutual alignment to be exact to avoid a loss in flux in the side branch. Overall, the alignment is less forgiving, vibrations can cause fluctuations in the downstream photon flux and need to be kept at a minimum. However, after talking to the staff at both existing and planned stations we were reassured that modern alignment systems are very well capable of providing the necessary accuracy and stability (personal communication at APS/ChemMatCARS with Yu-Sheng Chen, Mati Meron and Binhu Lin).

It remains an important point that a high-quality $C^*(111)$ will be challenging to source. Existing beamlines employ HPHT type IIa diamonds with a (111) face parallel to the largest surface. Chemical vapour deposition (CVD) grown single crystals were initially suggested as

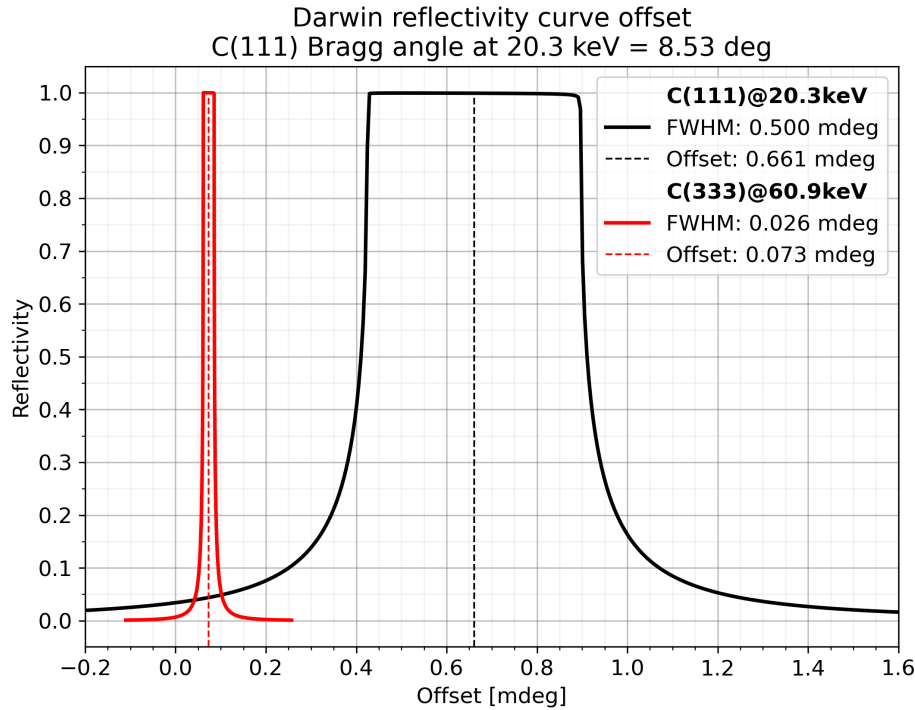


Figure 9: Comparison of $C^*(111)$ Darwin widths and reflective offsets of the fundamental wavelength and the first higher order component in angular space.

makeshift crystals that could be replaced as high-quality HPHT crystals become available. The implications to the main branch is expected to be low *i.e.* DanMAX already employs several CVD diamonds with a normal or 45 deg. incidence without detrimental effects to the beam quality. However, the resulting flux penalty that originates in lower crystal quality of CVD crystals was however deemed too big, making this route nonviable. The current situation for sourcing HPHT type IIa has greatly improved in recent months, making

2.4 Beam focusing

Compound refractive lenses (CRLs) provides a variable focus at the sample position. CRLs are popular for focusing X-rays due to their stability, relatively large aperture (beam acceptance), compact size and ease of alignment. Focusing CRLs are in-line optical elements *i.e.* that do not deviate or deflect the X-ray beam, which is a major advantage over mirror-based solutions for high throughput instruments. The main drawback of CRLs are their chromatic properties *i.e.* the strong variation of the refractive index as a function of photon energy. This requires a varying number of lenses in the beam path to maintain a constant focal distance and size. The usual implementation is a grouping of individual lenses, as schematized in Figure 10. Bi-concave lenses are usually packaged in individual lens lets, that are mounted in cassettes that are inserted into a V-block and aligned to be coaxial to the photon beam. The focal length of a stack of bi-concave lenses can thus be well approximated by $f = R/(2N\delta)$, where R is the radius of curvature, N is the number of lenses and δ is the refractive index decrement.

Despite of the beamsplitter in Bragg geometry not intrinsically focusing, unlike in Laue

geometry, it still produces astigmatism due to deformation under heat load. The effects of deformation on the beam are more pronounced in Bragg geometry due to the more grazing incidence. This generates an astigmatism that needs to be addressed in the design of the CRL. A stack of two-dimensionally focusing lenses has to be complemented by a stack of horizontally focusing one-dimensional lenses compensating for the astigmatism.

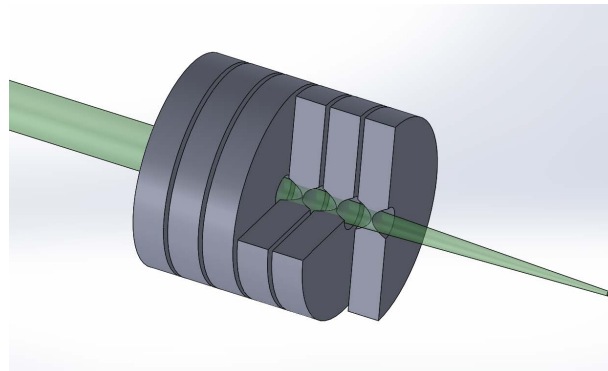


Figure 10: Schematic view of focusing CRL elements (figure from DanMAX DDR¹).

The beam sizes mentioned in this work are listed in full-width half-maximum (FWHM) in the horizontal times vertical direction. The unfocused beam profile at the sample position is shown in Figure 12 and is around $0.35 \times 0.45 \text{ mm}^2$ (FWHM, H×V) which is relatively unchanged at all photon energies (see Appendix B, Figure 52.6). The material choice in the ray tracing simulations in present work was performed primarily with beryllium, which has a low attenuation (absorption) of the transmitted photons and a relatively high refraction. Beryllium is widely employed at synchrotron beamlines, although other materials are also available at this energy range.¹⁷ Especially single-crystal diamonds are emerging as an attractive alternative, despite a higher absorption compared to beryllium, the larger refractive index means that fewer lenses are required.¹⁸ The use of C* lens elements was strongly encouraged by the DanMAX steering group, not only to plan for future upgrades and put focus on flexibility but as well to thoroughly examine the lenses, as they are an attractive upgrade solution for already existing transfocators.

Part III & IV in the MASH/Shadow report (Appendix B) explore the CRL combinations for achieving the different cases at the sample position, optimized for the various cases 1 through 5. The five cases are summarized in Table 6, with SINCRYS requiring two different types of lenses, to correct for aberrations introduced by the beamsplitter. The ray-tracing simulations are evaluated against five cases *i.e.* best focus (#1), a sample focus of $5 \times 5 \mu\text{m}^2$ (#2), a sample focus of $15 \times 15 \mu\text{m}^2$ (#3), a sample focus of $100 \times 100 \mu\text{m}^2$ (#4) and the natural, unfocused beam at the sample position.

The simulation was optimized for a minimal number of lenses for spatial and economic constraints. The difference in throughput between different lens element types are small, as the lens apertures are larger than the beam. This corresponds thus to up to 34 2D elements with a $R = 100 \mu\text{m}$ and two 1D elements with $R = 200 \mu\text{m}$. Considering the two scan cases with and without heat load (see Appendix B, Table 42.1 and Table 42.2), the 1D lenses account for the thermal deformation of the BS.

The best focus is thus $15 \times 5 \mu\text{m}^2$ with a beam divergence of $190 \times 130 \mu\text{rad}$ (H×V) and a flux of up to $1.2 \times 10^{13} \text{ ph/s}$ at a bandwidth of about 1.1×10^{-4} . For increased flexibility the

1D lenses allow to focus in the horizontal direction, but keep a moderate focus in the vertical. Thus, the number of 1D lenses increases for larger beam focus while the number of 2D lenses decreases. The beam profiles for the five cases are shown in Figure 11 and Figure 12 with field of views of $30 \times 30 \mu\text{m}^2$ and $700 \times 700 \mu\text{m}^2$, respectively. The red squares indicate the virtual apertures the flux is counted in Table 6. For the "best focus" and "unfocused" case the $5 \times 5 \mu\text{m}^2$ and $100 \times 100 \mu\text{m}^2$ aperture is chosen to guide the eyes.

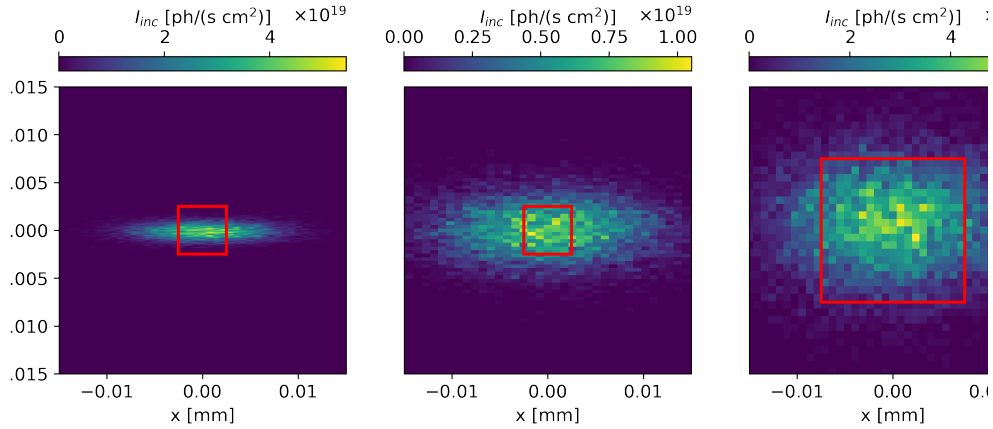


Figure 11: Beam profiles with a $30 \times 30 \mu\text{m}^2$ field of view at sample position with a photon energy of 21.80 keV. Left: Case #1, Best focus, Middle: Case #2, $5 \times 5 \mu\text{m}^2$, Right: Case #3, $15 \times 15 \mu\text{m}^2$.

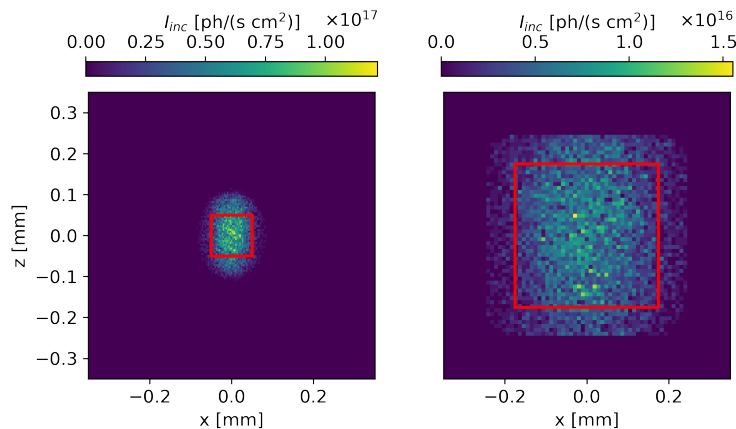


Figure 12: Beam profiles with a $700 \times 700 \mu\text{m}^2$ field of view at sample position with a photon energy of 21.80 keV. Left: Case #4, $100 \times 100 \mu\text{m}^2$, Right: Case #5, Unfocused.

A beamsplitter in Laue geometry would have an asymmetric reflection, leading to a large aberration, and was thus evaluated separately in the ray-tracing simulations. Considering the choice between a Laue and Bragg beamsplitter, the resulting in-focus beam flux is shown in Figure 13. In the Laue configuration, the number of lenses is increased to 34 2D elements and 5 1D elements for a $50 \times 5 \mu\text{m}^2$ (FWHM) beam focus with a beam divergence (FWHM) of $160 \times 130 \mu\text{rad}^2$ ($\text{H} \times \text{V}$), due to the large aberration of the asymmetric diffraction in Laue

Table 6: CRL combinations for Bragg-configured beamsplitter. The 2D lenses $R = 100 \mu\text{m}$, 1D $R = 200 \mu\text{m}$. The listed flux is also found in Figure 13b. Beam sizes are listed in FWHM, H×V.

	Best focus	$5 \times 5 \mu\text{m}^2$	$15 \times 15 \mu\text{m}^2$	$100 \times 100 \mu\text{m}^2$	Unfocused
20.00 keV					
# 2D	25	24	24	18	0
# 1D	2	5	6	0	0
Flux before [ph/s] ¹	1.3×10^{13}	1.3×10^{13}	1.3×10^{13}	1.3×10^{13}	-
Flux after [ph/s] ¹	5×10^{12}	5×10^{12}	8×10^{12}	8×10^{12}	-
Beamsize [μm^2]	14×5	14×5	19×5	120×130	450×350
21.80 keV					
# 2D	29	28	28	21	0
# 1D	2	6	7	0	0
Flux before [ph/s] ¹	8×10^{12}	8×10^{12}	8×10^{12}	8×10^{12}	-
Flux after [ph/s] ¹	5×10^{12}	5×10^{12}	7×10^{12}	6×10^{12}	-
Beamsize [μm^2]	14×2	13×2	15×5	120×130	450×340
23.00 keV					
# 2D	32	31	31	23	0
# 1D	2	7	8	0	0
Flux before [ph/s] ¹	6×10^{12}	6×10^{12}	6×10^{12}	6×10^{12}	-
Flux after [ph/s] ¹	2×10^{12}	2×10^{12}	5×10^{12}	5×10^{12}	-
Beamsize [μm^2]	16×5	14×5	15×5	125×130	450×340

¹ Before and after refers to the beam aperture defined for the column.

geometry. As the horizontal focal spot size is close to $50 \mu\text{m}$ which greatly exceeds that for the Bragg BS, a considerable loss in flux is observed in a $5 \mu\text{m}$ aperture at the sample *i.e.* at maximum $5.5 \times 10^{12} \text{ ph/s}$. This is a strong argument for choosing a beamsplitter in a Bragg geometry.

The best focus in the Bragg geometry creates a focal spot at the sample with dimensions of $15 \times 5 \mu\text{m}^2$ (FWHM, H×V), as seen as a function of energy in Figure 14. The beam divergence (FWHM, H×V) in the focal spot is $170 \times 100 \mu\text{rad}^2$ (see Appendix B), with a maximal flux of $1.2 \times 10^{13} \text{ ph/s}$ at a bandwidth of 1.1×10^{-4} . The saw-tooth shape are caused by the number of CRLs to achieve the focus with varying energy.

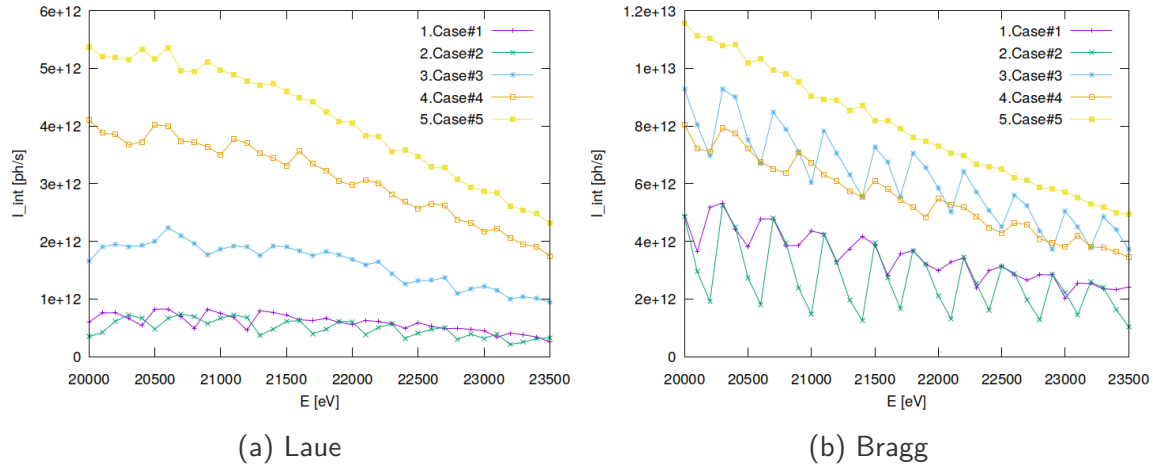


Figure 13: Photon fluxes at the sample position for a beamsplitter in Laue (a) and Bragg (b) configuration. Case #1: smallest focus with $5 \times 5 \mu\text{m}^2$ aperture, case #2: defocused to $5 \times 5 \mu\text{m}^2$ through $5 \times 5 \mu\text{m}^2$ aperture and case #3: defocused beam to $15 \times 15 \mu\text{m}^2$, case #4: defocused beam to $100 \times 100 \mu\text{m}^2$ & case #5: unfocused beam.

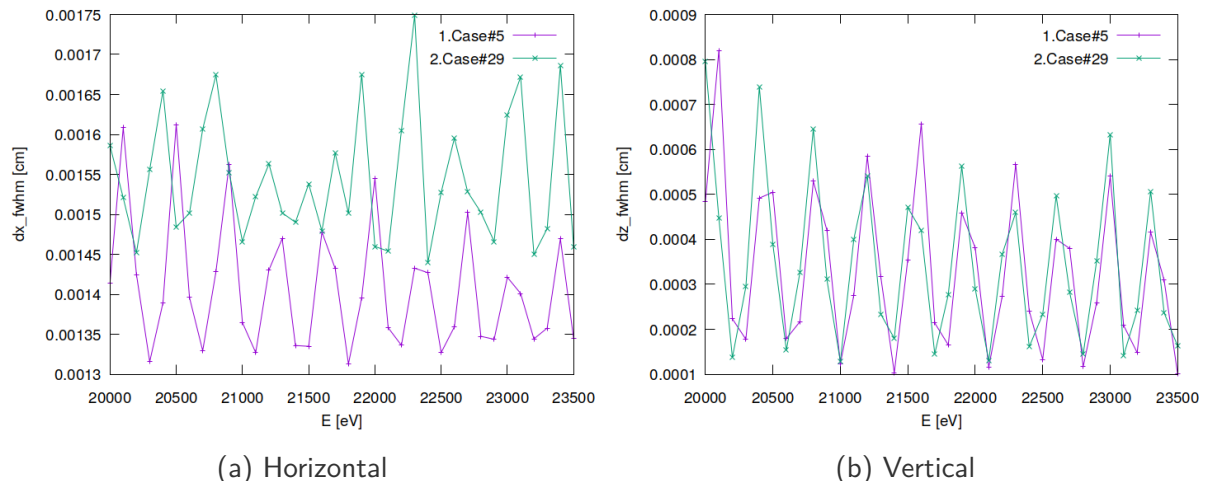


Figure 14: Best beam focus for the BS in Bragg geometry with (case #29) and without (case #45) heat load.

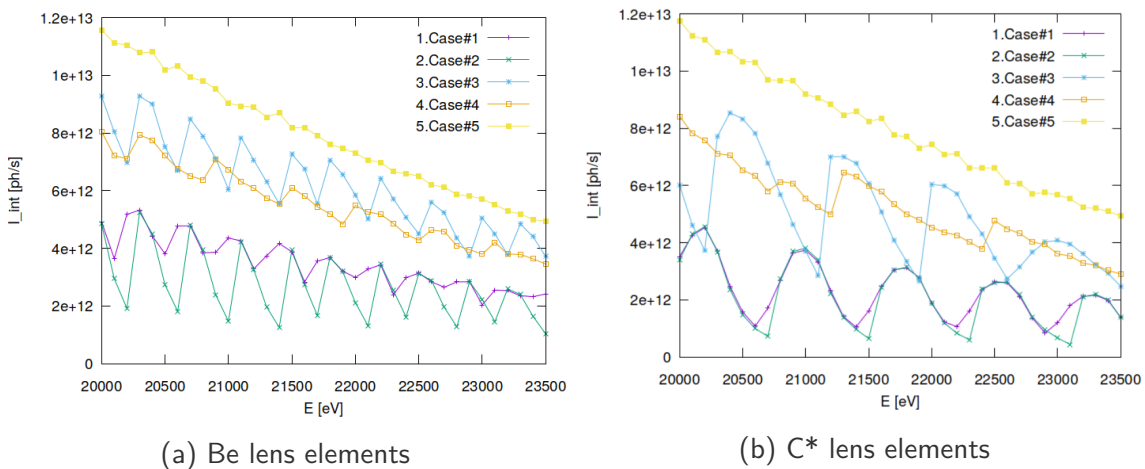


Figure 15: Photon fluxes at the sample position for a beamsplitter Bragg configuration and Be (a) or C* (b) lens elements used as transfocator. Case #1: smallest focus with $5 \times 5 \mu\text{m}^2$ aperture, case #2: defocused to $5 \times 5 \mu\text{m}^2$ through $5 \times 5 \mu\text{m}^2$ aperture and case #3: defocused beam to $15 \times 15 \mu\text{m}^2$, case #4: defocused beam to $100 \times 100 \mu\text{m}^2$ & case #5: unfocused beam.

Recent advances in the manufacturing process of C* lenses render them an attractive alternative to Be. The refractive index of C* is higher compared to Be, the ratio between δ for Be and C* is about 2.14 at 20 keV, meaning about half the number of lenses is required when using a radius with a similar focusing power. As absorption is higher in C*, the resulting flux at the sample position (using the optimal number of lenses for the respective material) is approximately 15% lower for C* than for Be (compare Figure 15). However, it is noted that Be-lenses inherently scatter from grain boundaries and defects because of their poly-crystalline nature and the mechanically imprinted lens profile results in density fluctuations throughout the lens element. These aspects have not been modelled in the ray tracing simulation as it assumes a perfect crystalline structure. Diamond lenses can be made from high-pressure high-temperature (HPHT) grown synthetic diamonds that are basically single-crystals with only few dislocations. Recently, lenses were presented that show a surface quality and slope errors comparable to the existing Be lenses.¹⁸ The parabolic lens shape is created by laser ablation and a subsequent mechanical polishing results in highly promising lens properties. The lower intrinsic scattering and higher beam quality from a more homogeneous density through the C* optical component is highly beneficial for the possible future imaging application of the side-station. In conclusion, the C* elements lower intrinsic scattering and higher precision might be well worth the 15% lower flux. The number of required 2D and 1D lens elements to achieve the requested focus is roughly half for C* (2D: 8 - 14, 1D: 0 - 4) compared to Be (2D: 18 - 32, 1D: 0 - 8). However, fewer lens elements result in larger fluctuations due to the larger step size in focal length adjustment.

2.5 Heat load management

Absorption of synchrotron radiation in an element enforces a certain heat flux distribution. The beam splitter is exposed to a significant power and the resulting thermal effect must be

considered. The worst case with respect to the incident power corresponds to the minimal undulator gap of 4.4 mm which results in around 40 W incidence flux on CM1 after the high pass filters (HPF). The BS is thin and has a relatively small Z (carbon) so the absorbed flux remains relatively small, in the same order as the existing HPF of 1.0 mm diamond. The existing solution for water cooling of the two HPFs is expected to be sufficient to supply adequate cooling for CM1, but extra ports should be installed in the OH.

The cooling design of the beamsplitter is similar to that of a thin filter. In the simulations the thin crystal slab is mounted on a thick plate of oxygen-free copper with a hole in the middle to pass the beam. The hole should be of minimum size to keep cooling pathways short and thus the peak temperature low. Despite of the high thermal conductivity, heat transport across the crystal slab is not efficient given its thickness. The crystal slab is clamped in place by a small copper frame ensuring good thermal contact to the plate. A copper pipe loop for cooling is brazed onto the copper plate keeping roughly the same distance to the hole in three out of four directions. The distance to the hole is not very critical here thanks to the good heat transport in the thick copper plate. While the BS is thin, the beampath through it varies from 0.664 mm to 0.764 mm for the lowest and highest energy, respectively, due to the angle of incidence to the white beam.

In the FEA of the heat transfer, heat removal by the cooling agent is simplified by assuming a constant heat transfer coefficient of 1 W/(K cm²) to a cooling agent reservoir of constant temperature at 293.15 K. The chosen heat transfer coefficient is typical for turbulent flow.

In this configuration the incident irradiance at the CM1 C* surface and the absorbed power is shown in Figure 16.a (simulated for 21.80 keV). The absorbed irradiance on the surface of the fixture and cooling tubes is negligible (see Appendix B). The temperature on the surface of the C* is shown in Figure 16.b.

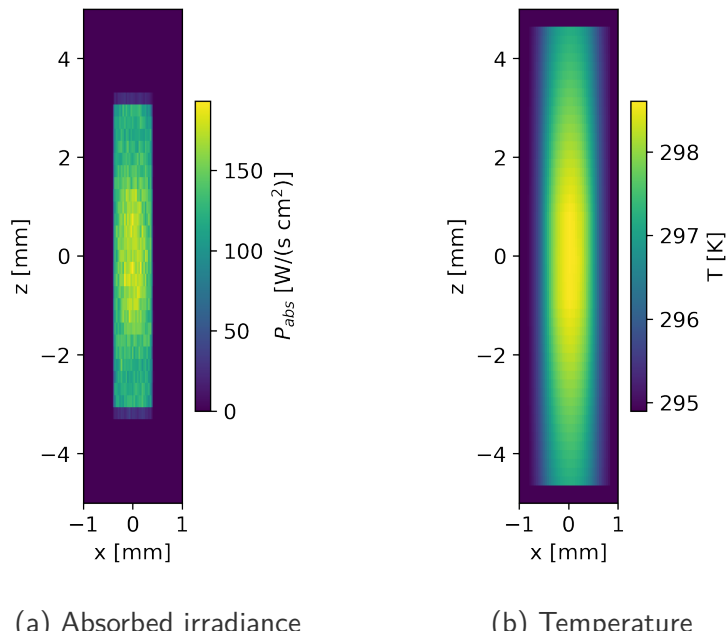


Figure 16: Absorbed power and surface temperature of CM1 in Bragg geometry at 21.80 keV.

In summary, using C*(111), either in Laue or Bragg geometry, is the best option. The

flux in the monochromatic beam is comparable to that of cryo-cooled Si(111). The irradiance that is forwarded towards the rest of the SINCRYS components is monochromatic and limited by the DW of diamond, and thus no active cooling is required. For the crystal mount design, care should be taken in the assembly to reduce thermal time constants and to avoid heating of components due to secondary scattering. Zhu *et al.*⁶ reported improved thermal conduction between the thin crystal and the mounting frame, by using an all diamond design with the beamsplitter held by perforated diamond micro-clips in a CVD diamond frame.

2.6 Vacuum system

The vacuum system for SINCRYS (and DanMAX) are sketched in Figure 17. The monochromators are located in chamber A and C for CM1 and CM2, respectively, with a wedge-shaped transfer pipe, B, between them that accommodates the varying Bragg angles. The transfocator (D) is a long chamber containing the cassettes for the CRLs and translations to align them. A diagnostic module with a beam viewer and in-vacuum slits should be installed between C and D. The beam safety shutter (BSS) should be installed as the last module before the wall, parallel to the DanMAX BSS. The vacuum ends inside the EH with a diamond window.

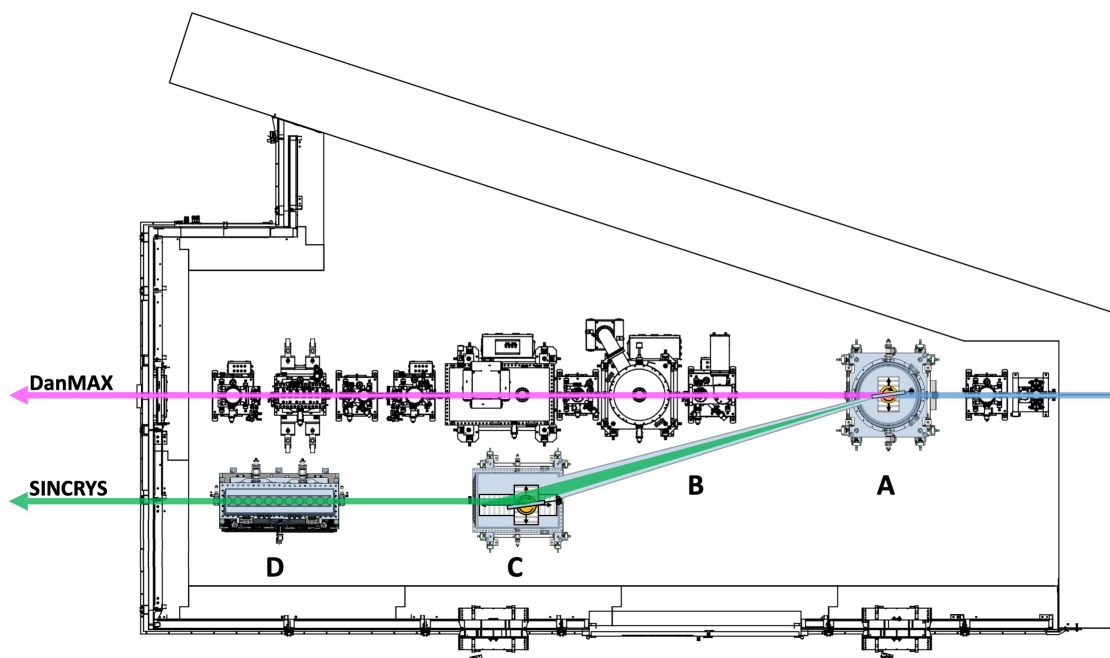


Figure 17: Sketch of the hutch space showing limitations and requirements of the side branch. A: Ultra-high vacuum chamber containing the beamsplitter CM1. B: High vacuum beam pipe. C: High vacuum chamber with the long translation stage of the second crystal monochromator CM2. D: Long chamber containing all focusing elements (CRL). The existing DanMAX optics is photographed in Appendix A, Figure 29 and Figure 31.

The component positions are listed in Table 7 with the distances along the SINCRYS beampath, and the parallel position on the white beam axis. The precise position of the BS CM1 has some play which should be chosen such that the B pipe is least intrusive to

serviceability of ports for the DanMAX white beam slits and hDCM. Consequently, the relative position to CM2 must follow.

Table 7: Positions of SINCRYS Optics with a photon energy of 20.00 keV (CM2 at lower boundary). The listed Z positions are all along the white beam axis.

Component	From source [mm]	Z position [mm]	Y position [mm]	Travel along Z [mm]
IVU16	0	0	0	-
FE-OH Wall	-	-	-	-
Trigger unit	22750.0	22750.0	0	-
Collimator	23300.0	23300.0	0	-
HPF1	23474.8	23474.8	0	-
HPF2	23484.8	23484.8	0	-
BS CM1	24850.0	24850.0	0	-
CM2	28506.0	28058.1	1000	0 – 600.0
Diagnostics	-	-	1000	-
CRL1	31500.0	31360.6	1000	-
CRL2	31600.0	31460.6	1000	-
BSS	32000.0	31860.6	1000	-
OH-EH Wall	32500.0	32360.6	1000	-
EH conditioning	33000.0	32860.6	1000	-
Sample	34000.0	33860.6	1000	-

All of the components should comply with the electrical standards and mechanical stability (all eigenfrequencies must be kept above 55 Hz, adhering to the MAX IV general goal of a factor of 3 more than the 5–18 Hz from the nearby E22 highway). For the vacuum system, the extracted beam will exit the DanMAX vacuum and enter a separate vacuum system for SINCRYS, as the DanMAX optics are all directly connected to the MAX IV machine vacuum.

The beamsplitter is situated inside the DanMAX vacuum vessel, and thus should fully comply with the general MAX IV standards for ultra high vacuum (UHV, $P < 5 \times 10^{-9}$ mbar), separate from the rest of the SINCRYS vacuum vessel. The separation between the vacuum vessels can be achieved either by a small air gap with two X-ray windows or a sealed connection using a single vacuum window to avoid the travel through air. The loss in flux through air scattering is considered low given the energy of 21 keV, however, the variation of the exit angle over the full energy range is small and a single window solution is preferable.

There are no requirements to preserve coherency in the branched beam for the SINCRYS side station, yet, future upgrades and additions might want to make use of the beam quality. To not limit these aspects the window should be at least a polished, poly-crystalline CVD diamond and preferably single-crystalline. The SINCRYS vacuum vessel will only need to be built as an high vacuum (HV) chamber, in contrast to the UHV of the main branch. In general, the SINCRYS vacuum should reach a level of 1×10^{-8} mbar within a reasonable degassing period. The system should be equipped with roughing valves and vacuum gauges. The beam

transfer vacuum ports should be a ConFlat CF40 with rotatable ports at the upstream side, and rotatable or fixed ports on the downstream side (except for the beam transfer between the crystal monochromators, that should include a vacuum valve and bellows).

This scheme simplifies dependency and compatibility concerns of the two stations and allows work to be performed on the side branch without major interference. The shared OH design renders neither beamline operational while work is performed on either, however, the strict separation makes the vacuum systems less susceptible to outage.

Due to the span in Bragg angles with varying X-ray energy (as a result of changing undulator gaps) the beam-pipe connecting CM1 and CM2 (B in Figure 17) be designed with a wedge shape, expanding linearly in width while approaching CM2. The design and type of connection between the vacuum vessel of CM2 and the beam pipe will need some additional attention. In the eventuality the larger DanMAX vacuum vessels need to be serviced, it should be possible to temporarily remove the transfer pipe between CM1 and CM2. The DanMAX optics are generally designed for serviceability from the inboard side *i.e.* the opposite side of the SINCRYS equipment, with the exception of a small number of vacuum ports on the outboard side. Similarly, SINCRYS should strive for the same, but to the outboard side. Appendix A.2 includes some CAD renders of chambers A, B and C. The render is designed such that the scattered beam is always minimum 10 mm from the chamber wall.

To simplify operation and alignment of CM2, chamber C should include a number of ports providing a clear view towards the outboard plane of the vacuum chamber and CM2 stage. The outboard side of the chamber should have a view flag consisting of a coating of a UHV compatible phosphor highlighting the current beam position in the non-aligned state. This low-tech tool to visualize the beam position at CM2 position helps alignment enormously and is inspired by the ChemMatCARS beamline design at the Advanced Photon Source (APS) of the Argonne National Lab (ANL).

2.7 Mechanical translations & specification

2.7.1 Crystal monochromator 1

In the previous section some of the required motions for the two monochromators CM1 and CM2 were already mentioned. CM1 is characterized with two rotation axes (yaw/roll) to adjust for the Bragg angle and vertical beam steering. The remaining axis (pitch) is considered a non-critical motion and is therefore not required to have active motorization. Nonetheless, mechanical alignment must be provided and it should come pre-aligned with the mount. The allowed range of motion for adjusting the Bragg angle of CM1 in combination with the length of the translation stage and motions of CM2 set the boundaries for the energy range available at the SINCRYS station. The needed angular range is relatively small (between 7 – 9 degrees). Table 8 lists the anticipated specifications for CM1 including their respective precision.

Note a vertical actuator/translation is included for the diamond crystal to allow for a parking position for the crystal fully extracted from the white beam. This is to allow the full white beam to pass through unhindered by the BS. If absorption of CM1 would dampen the DanMAX beam by more than a few percent one of the two high-pass filters (HPF, 0.6 and 0.4 mm thick Diamonds) can be removed this requires the ability to re-insert a HPF, which can be achieved *e.g.* with PLC logic. A revolver, double-cassette layout or a separate vacuum

unit can ensure that either CM1 or this filter are in the beam to comply with the specified power load of the DanMAX white beam stop.

Table 8: Motion specifications for the beamsplitter.

Beamsplitter Monochromator (CM1)

Bragg Yaw coarse	Ry	range resolution repeatability	7 – 9.0 deg $< 2 \mu\text{rad}$ $< 1 \mu\text{rad}$
Bragg Yaw fine	Ry	range resolution repeatability	150 μrad 0.01 μrad 0.05 μrad
Roll coarse	Rz	range resolution repeatability	$\pm 10 \text{ mrad}$ $< 8 \mu\text{rad}$ $< 2 \mu\text{rad}$
Roll fine	Rz	range resolution repeatability	150 μrad $< 0.01 \mu\text{rad}$ $< 0.05 \mu\text{rad}$
Translation ¹	Ty	range resolution repeatability	-30 – 0 mm $< 1 \mu\text{m}$ $< 2.5 \mu\text{m}$

¹ A vertical translation should allow to fully extract CM1 (beamsplitter) from the direct beam path. In this configuration it is translated down for stability.

Both the crystals CM1 and CM2 must accept the full beam footprint in the aligned state. The dimensions of the defect-free area are thus suggested to be no smaller than 1 mm in the Y-direction (vertical, height) and 8 mm in the X-direction (horizontal, length) for the crystals.

2.7.2 Crystal monochromator 2

The second Bragg stage for CM2 should be on top of a carriage mounted to a long, linear translation. In addition to the long linear translation, the goniometer should have both horizontal and vertical translations to offset the beam perpendicular to the beam direction and compensate for misalignment over the long linear translation, yaw (Bragg angle, both coarse and fine) and roll (coarse and fine). The specifications for CM2 are listed in Table 9. Since the crystal is only exposed to monochromatic radiation no cooling is required.

Table 9: Motion specifications for the CM2 goniometer.**2nd Monochromator**

Translation ¹ Tz	range resolution repeatability	0 – 600.0 mm < 2.0 μm < 5.0 μm
Translation Tx	range resolution repeatability	± 1.0 mm < 2.0 μm < 2.0 μm
Bragg Ry Yaw coarse	range resolution repeatability	7 – 9.0 deg < 2 μrad < 1 μrad
Bragg Ry Yaw fine	range resolution repeatability	150 μrad < 0.05 μrad < 0.05 μrad
Roll Rz coarse	range resolution repeatability	± 20 mrad < 8 μrad < 2 μrad
Roll Rz fine	range resolution repeatability	150 μrad < 0.05 μrad < 0.05 μrad

¹ The long Tz range covers the corresponding θ difference between 20.30 – 23.00 keV with a 1.0 m offset to the main branch.

2.7.3 Transfocator

The design of the transfocator can be based on the concept already installed at DanMAX. DanMAX has a transfocator that consists of 50 beryllium (optical grade O-30-H) with $R = 200 \mu\text{m}$ that can be inserted to the beam path in a binary fashion (cassettes of 1, 2, 4, 8, 16, 19 CRLs), to minimize the number of actuators required. The individual cassettes are pneumatically actuated. The lenses (and pinholes at the front and back of each cassette) are fixed by a spring-loaded clamp with the whole cassette being driven into a base V-block along the beam path, ensuring a high repeatability.

The transfocator should be designed such that it is possible to align the transfocator axis to the photon beam at SINCRYS, with two motorized linear translations along X and Y (perpendicular to the beam axis). There should be two motorized rotations, pitch and yaw (around the X and Y axes). The motions should include absolute linear/rotary encoders as specified in the MAX IV motion standards. The foreseen ranges and specifications are listed in Table 10. Vacuum ports along the photon beam shall be CF40 with rotatable ports at the upstream side, and fixed or rotatable at the downstream side.

Table 10: Motion specifications for the transfocator. All motor positions should have encoders.

CRL (transfocator)

Translation Vertical	Ty	range resolution repeatability	±5.0 mm < 2.0 µm < 5.0 µm
Translation Lateral	Tx	range resolution repeatability	±5.0 mm < 2.0 µm < 5.0 µm
Yaw	Ry	range resolution repeatability	±10 mrad < 10.0 µrad < 10.0 µrad
Pitch	Rx	range resolution repeatability	±10 mrad < 10.0 µrad < 10.0 µrad

2.8 Beam diagnostic and shutter modules

There are no special requirements for the beam shutter at SINCRYS and the design from any of the monochromatic beam shutters currently active at MAX IV can be used.

The beam diagnostic modules should include beam slits after the CRLs, beam intensity monitor and viewers. The concepts can similarly take basis in the existing devices from the existing solutions at DanMAX, aside from the much simpler heat dissipation after extracting the monochromatic beam from the white beam.

For the beamviewer and intensity monitor, the general concept from DanMAX is depicted in Figure 18.¹ A fluorescent diamond crystal (fluorescence screen) is vertically inserted with a pneumatic actuator at 45 degrees to the incident beam in the vacuum vessel. A silicon photodiode monitors the intensity of the scattered radiation coming from the diamond crystals. The beam position is monitored with a power-over-ethernet (POE) camera through a viewport. According to the existing DanMAX beamviewers, the beam position can be monitored to a precision better than 10 µm with the fluorescent screen and in-air POE camera.

A beamviewer has not been inserted between CM1 and CM2, as the viewflag will qualitatively help to locate the beam in the unaligned state. Furthermore, a viewport could optionally be directed towards the diamond window separating the DanMAX and SINCRYS vacuum vessels. In the SINCRYS beampath one beamviewer should be placed between CM2 and the CRL stacks and a final one in the experimental hutch for which no final decision is made on the placement.

2.9 Radiation safety

Since there are no modifications to the FE of DanMAX and the transmitted power to the SINCRYS branch through the beamsplitter is relatively moderate, there is no expectation for

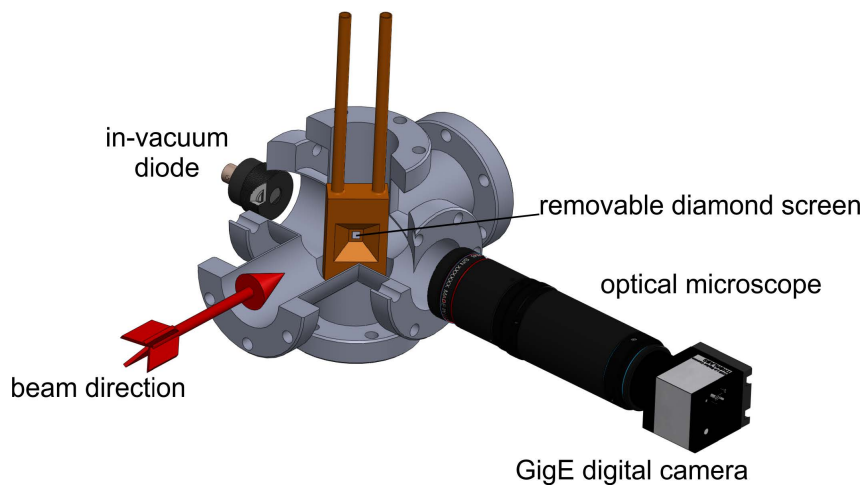


Figure 18: Concept for beam diagnostics at DanMAX, allowing a direct view of the beam *via* the in-air POE camera and a diode detector. The diamond crystal has a 45 degree incidence to the beam, and has a vertically pneumatic actuator to remove it completely from the beampath. An in-vacuum silicon diode monitors the X-ray intensity. Figure from DanMAX DDR¹.

further radiation shielding. That is, a standard MAX IV beamshutter will be installed at the beam transfer between the OH and EH2 (SINCRYS EH). The last two modules at the wall to the EH is thus the CRL unit and beam safety shutter.

The final assessment for the radiation shielding will be performed in 2023 at MAX IV. The radiation safety simulations have already been performed for the SINCRYS EH, but the changes to the OH in particular have to be incorporated. No major changes are foreseen.

2.10 Effect of beamsplitter on transmitted beam to DanMAX

The C* beamsplitter has a minimal effect on the transmitted white beam that continues to the DanMAX station. Refractive effects are negligible due to carbons tiny refractive decrement at these energies, the fact that there are only two surfaces which are hardly bent and if so, are mostly parallel. Temperature gradients inside the diamond sheet are small, and with its thickness gradients, thanks to diamond being the material with the highest thermal conductivity. Above that, any thinkable refractive effects would occur with commonly used diamond filters, too. The beam diameter 10 metres downstream of the BS is the same with and without accounting for heat deformation within noise level.

Absorption in CM1 is significant for the transmitted beam, however. Overall, the absorption above 15 keV is small at approx. 1 – 2% in Laue geometry and approx. 10% for 100 micron thick diamond slab in Bragg geometry (see Appendix B, Figure 34.32). The considerably higher absorption in Bragg geometry is simply because of the longer path length in the beamsplitter due to the shallower incidence, as the path length through a crystal with thickness t is thus $t/\sin(\Theta_B)$. With a thickness of $t = 100 \mu\text{m}$ and the lowest Θ_B of 7.52 deg., the effective beam path is 758 μm , which is comparable to the thickness of the existing DanMAX high pass filters at a thickness of 600 μm (first HPF) and 400 μm (second HPF).

Nevertheless, the beamsplitter can significantly affect the transmitted beam, if by chance the same undulator harmonic is used at both stations. Small changes in the Bragg angle of the beamsplitter can have a considerable change in flux to also the transmitted beam, which is highly undesirable and easily avoided. The beamsplitter has a reflectivity close to 100% in the narrow spectral window it is set up for, thus effectively depleting the main beam of photons inside that window.

Far from fulfilling the Bragg condition, *i.e.* if using a different harmonic in the main branch, the beamsplitter simply acts as a refractive element, altering the transmitted beam by refraction and absorption only.

2.10.1 Absorption in high-pass filters

As the incidence is relatively low for the BS in Bragg geometry, the path length through even a thin slab of C* is comparable to the existing upstream HPFs at DanMAX. The transmitted, absorbed flux in the BS is low (approx. 10%) and decreases with increasing energies. This is easily compensated by removal of one of the upstream HPFs, that have thicknesses of 0.4 and 0.6 mm. It should be noted, however, that the downstream optical components at DanMAX are designed for an exposure that does not exceed the transmission as defined by the two current HPFs. Having a parking-position for the SINCRYS C* thus must compensate for the increased flux reaching the optics, by re-inserting a HPF. This can be achieved *e.g.* with a pneumatic actuator close to the SINCRYS beamsplitter, with a PLC logic that ensures that either the SINCRYS beamsplitter or the second HPF is in the beam path.

Figure 19 shows the effect on the photon flux at the position of CM2 by removing the 0.6 mm HPF and both filters, with CM1 in the Bragg configuration. Case #3 is with only the 0.4 mm HPF and case #4 is without both of the upstream filters. Removing only one filter is insignificant for the SINCRYS flux (it is actually slightly increased), whereas it might regain some of the DanMAX flux that is absorbed in the long beampath through the BS. Removing both filters exposes the crystal to a significant heat load, as the BS now functions as a low

pass filter itself. The last case is evidently not a viable option, with also multiple indications of considerable beam distortions in the transmitted beam.

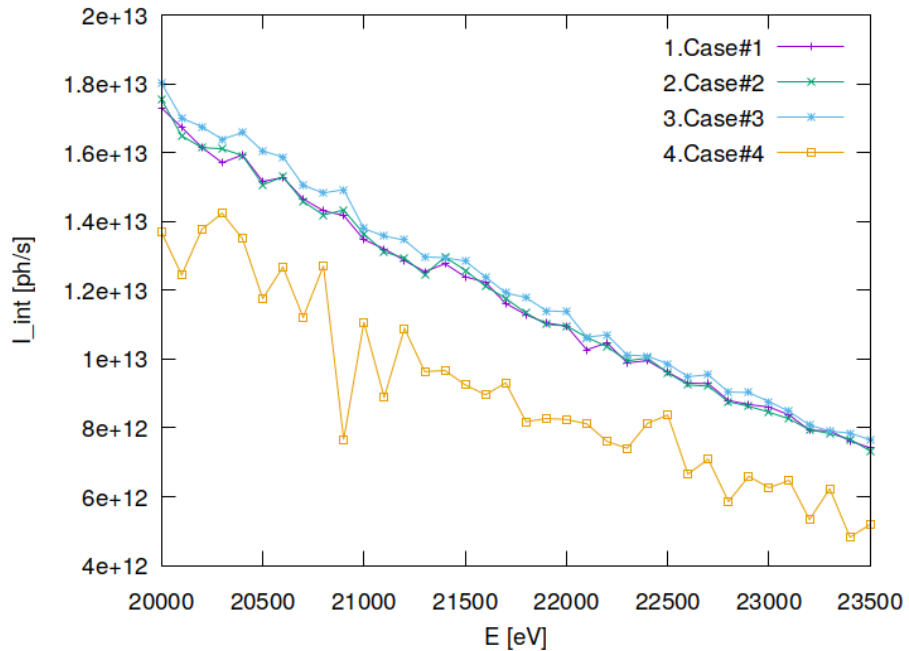


Figure 19: Photon flux at CM2. Case #1 is without heat load, case #2 is with heat load and both HPFs. Case #3 is only with the 0.4 mm HPF, and case #4 is entirely without the HPFs.

3 Experimental Hutch

The most upstream component in the EH is the diamond vacuum window. The sample position is at the beam focus, which is at 34000 mm downstream of the source, approximately 2500 mm downstream of the CRLs. A translatable "breadboard" table is suggested to house the beam conditioning unit (BCU), beam pipe a highly precise crystal goniometer and other viewers, beamstop etc.

The end station design is not completed and subject to change, it is included to give an overview of the current ideas.

3.1 Receiving beampipe and beam conditioning unit

The BCU can take inspiration from the design at DanMAX. When establishing the BCU for SINCRYS it will also be beneficial for both end-stations to ensure the components are interchangeable with DanMAX. The various optical components described in this section can be installed on an optical grade extruded aluminium profile for ease of placement and flexibility, such as X95 profiles from Newport. The beam conditioning unit of DanMAX is depicted in the photograph in Figure 20.



Figure 20: Beam conditioning unit at DanMAX. From upstream to downstream the last diamond vacuum window, a beam position monitor, fast shutter, beam absorber and reference foils, on-axis laser, in-air slits and beampipe that extends to the PXRD station.

In upstream-to-downstream these components should include the itemized list below. Some of the components will be described in further detail in the following subsections. The lengths are relatively conservative *i.e.* there is space enough (DanMAX BCU is approximately 50 cm long from beam position monitor to the slits at the beampipe).

- Fast shutter (10 cm)
- Motorized Slit system (10 cm)
- Pneumatically actuated attenuators (30 cm)
- Intensity monitor (10 cm)
- Sample (at 1.5 m)
- Motorized beam stop (within 10 cm of the sample)

A fluorescence-based "X-ray eye" should be developed, which can be installed on the diffractometer, as an "*ad hoc* beamviewer" at the sample position.

3.1.1 Fast shutter

The fast shutter should allow to quickly turn the beam on/off at the sample and detector positions. At DanMAX this has been implemented with a commercially available beam shutter for optical systems at visible wavelengths, but where the shutter has been replaced by a high- Z metal that absorbs X-rays.

3.1.2 Attenuators

Similar to the DanMAX attenuator system, a stack of attenuators are envisioned that can be actuated by a pneumatic system and operate in an accumulative fashion. The system is based on metallic foils with thicknesses between 25 and 100 μm . DanMAX has a total of 4 actuators in the vertical direction and 4 horizontal on a custom post, that has a total length of approximately 10-12.5 cm in length. 4 actuators thus achieves 2^4 different combinations attenuating the beam from 25% to 99.5% with the foils listed in Table 11. Lower beam intensities can be reached by installing another foil of 25 or 50 μm . However, DanMAX experienced the texture of the Ni attenuator foils to be highly textured, significantly impacting the transmitted beam profile. Alternatives should be mapped out for SINCRYS.

Table 11: Attenuator transmission with various thicknesses of Ni foil at 21.80 keV.

Thickness [μm]	25	50	100	200	400
Transmission [%]	57	32	10	1	0.01

3.1.3 Slit systems

One or two sets of motorized air-slits (or, preferably vacuum-compatible) should be installed at the entrance to the experimental hutch and as close to the sample as possible. In most situations, none of these slits should cut the incident beam diameter, and the second should only clean up scattering from the beam path.

3.1.4 Beam intensity monitor

A beam intensity monitor should be installed in the beam path downstream of the BCU. This could also serve as a beam position monitor.

3.2 Goniometer

The goniometer needs to meet the highly focused beam and to facilitate a short sample to detector distance. The latter is crucial to maximize achievable resolution while maintaining the necessary Omega, Chi (or Kappa) and Phi crystal rotations to thoroughly sample the reciprocal space. This translates to a compact goniometer design where the detector is able to approach the system to as close as 50 mm. The micron sized beam requires high positional accuracy and the sphere of confusion (SOC) of the scannable axis (Omega or Phi) must be less than 5 μm . Additionally, collisions are problematic at synchrotron facilities due to the mainly custom-made assembly of components. An automatic collision detection system would be a highly valuable feature of the goniometer and the detector. There are currently three options/vendors in discussion, the Arinax MD3 with the Mini-Kappa (MK3) goniometer head, the SmarAct SMARGON Microrobot and the Huber TS-63438 Kappa goniometer. The details are listed in Table 12. All three are compatible with automatic sample changer robots.

Table 12: Goniometer specifications.

		Arinax MD3 (MK3)	SMARGON Microrobot	Huber TS-63438
Sphere of confusion	[μm]	0.1	< 1.0	5-10
Angular resolution	[$\mu\text{°}$]	100	100	50
Angular velocity	[$\text{°}/\text{s}$]	720	180	-



Figure 21: Arinax MD3 Goniometer and Mini-Kappa (MK3) goniometer head. Figure credit: Arinax (<https://www.arinax.com/md3-high-precision-x-ray-microdiffractometer/>)

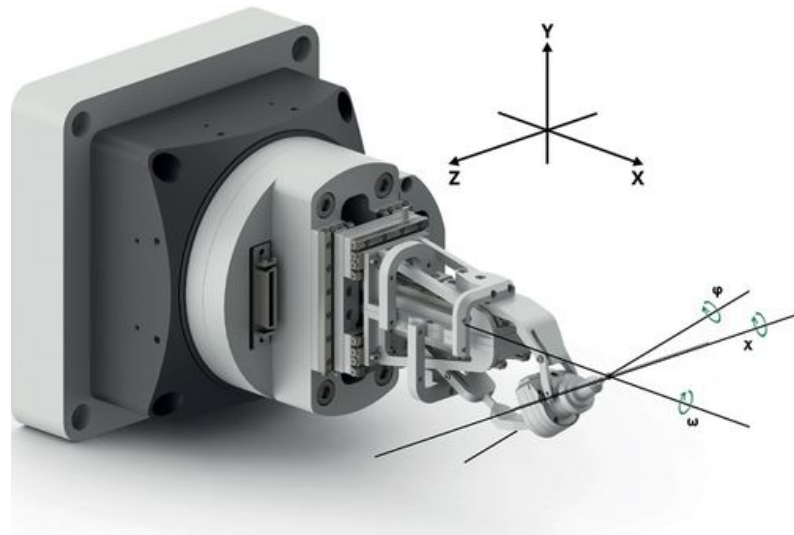


Figure 22: SmarAct SMARGON Microrobot. Figure credit: SmarAct (<https://www.smaract.com/en/smargon>)

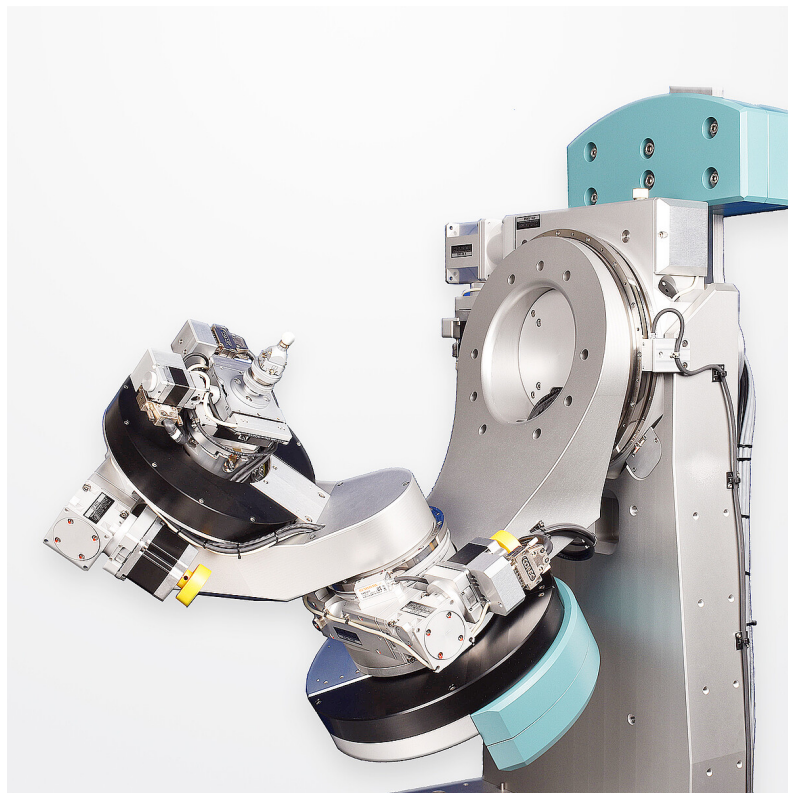


Figure 23: Huber Kappa goniometer TS-63438. Figure credit: Huber (<https://www.xhuber.com/de/produkte/1-komponenten/12-rotation/kappa-goniometer/>)

3.3 Detector

In the last decade the hybrid photon-counting (HPC) pixel array detectors (PAD) have matured and are now widely established at synchrotron facilities. This can be attributed two major factors; one being the large number of pixels (in the megapixel-range) covering a large area in reciprocal space and the second being the intrinsically fast and direct detection with a high efficiency allowing sub-millisecond timescales for the entire acquisition time for one frame.

The two most viable options foreseen for SINCRYS are the PILATUS3 X CdTe 1M (*i.e.* its successor PILATUS4, as PILATUS3 is discontinued September 2023) and the EIGER2 CdTe 4M detectors from DECTRIS AG. A comparison is given in Table 13. The nature of the single-crystal experiment is challenging to any type of detector due to the contrast between high- and low-intensity reflections recorded on the same image. This is different to a powder X-ray experiment, where the Bragg reflection is shared around the Debye-Scherrer ring that usually leads to lower intensities.

Table 13: Comparison of PILATUS3 and EIGER2 detectors.

	PILATUS3 X CdTe 1M	EIGER2 X CdTe 4M
Number of modules (W×H)	2 × 5	2 × 4
Active area (W×H) [mm]	168.70 × 179.40	155.10 × 162.15
Maximum frame rate [Hz]	500	500
Readout time [ms]	0.95	continuous
Maximum count rate [ph/s/mm ²]	3.4×10^8	1.7×10^9
Pixel array format (W×H) [px]	981 × 1043	2068 × 2162
Pixel size [μm]	172	75
Sensor thickness [μm]	1000	750
Weight [kg]	25	15.7

Another example is diffuse scattering that falls outside the reflections, either next to them or at any point in reciprocal space. Krause *et al.* recently reported on the these challenges as observed for a PILATUS3 detector,¹⁹ and many of the same challenges are carried over to the EIGER2 platform albeit the electronics are different (with EIGER2 being advantageous over PILATUS3 with reference to this challenge).

The quantum efficiency of the active detection modules depend on the stopping power of the material towards the X-ray photon. For photon energies of 20.0 keV the photon attenuation is dominated by the photoelectric effect. Upon absorption in the detector module, a proportional number of electron/hole pairs are created (about 4550 pairs for CdTe).²⁰ CdTe is often the material of choice at high-energy beamlines, including DanMAX which employs a DECTRIS PILATUS3 X CdTe 4M detector. The downside is the increased cost in manufacture of CdTe modules, when compared to the silicon counterparts. Since SINCRYST will have an energy close to 20 keV it is clear that a quantum efficiency above 90% is retained in the CdTe modules, compared to the silicon modules at approximately 30%, as they are compared in Figure 24, as 20-23 keV fits below the K_{α} of both Cd and Te, but significantly above Si.

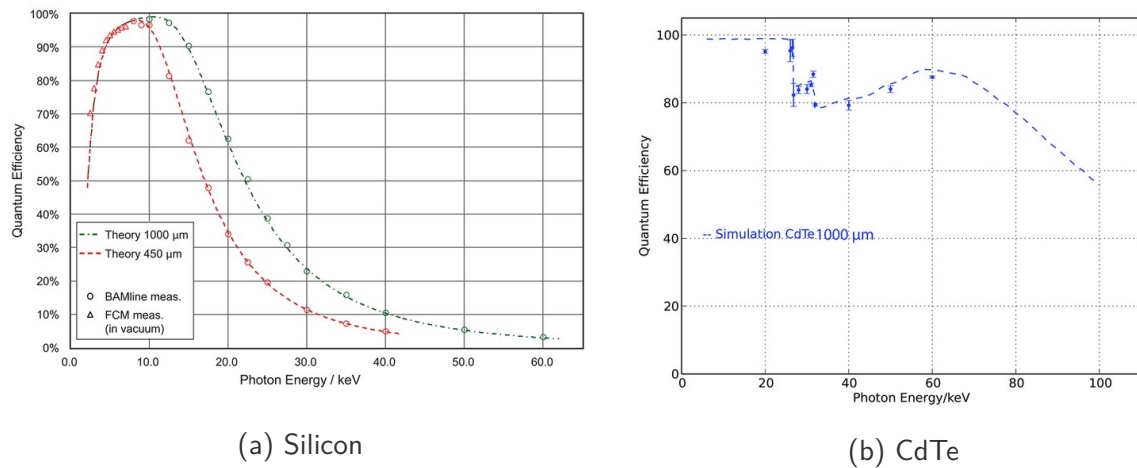


Figure 24: Quantum efficiency detector modules. Figure credit: DECTRIS AG (<https://dectris.com>)

In Summer 2022 an EIGER2 X CdTe 4M system was borrowed from DECTRIS for a direct evaluation and test of suitability of the two detector systems. Based upon the study by Krause *et al.*¹⁹ a FeSb₂ crystal was mounted on the 2D-powder X-ray diffraction station at DanMAX and exposed during a single, full ω scan with a photon energy of 20.0 keV. FeSb₂ is an ideal example of a small unit cell crystal with a high scattering power (high Z), *i.e.* with a small number of highly intense Bragg reflections. The energy was calibrated with a NIST LaB₆ line-position standard with a number of different sample-detector distances. The experiments were repeated with various absorbers to attenuate the beam.

Figure 25 shows the comparison of integrated, scaled, and averaged diffraction intensities of FeSb₂ collected with the PILATUS3 (P3) and the EIGER2 (E2) detectors. The scatter plot shows the relative difference between the two data sets, defined as the difference divided by the mean value as a function of the logarithm of the average intensity. In this plot, the allowed values range from -2 to 2 and a complete lack of bias is indicated by values close to zero. The scaling of the data for comparison is arbitrary, as is typically the case for X-ray diffraction data. The panels to the left of and below the bottom plot are histograms showing the distribution of data on the two axes. We tried to minimize deviations in the two experiments, using the exact same crystal, temperature, beam size and energy. However, due to the exchange of the two detectors it was impossible to maintain an identical crystal orientation. A direct comparison of the two sets of data will therefore always be a scattered distribution. Nevertheless, the absence of any systematic bias shows that the E2 data, collected with substantially less attenuation, do not suffer from the non-linearity issues at a much higher flux.

The experiments show that the E2 detector is capable of handling approximately 10 times higher flux without sacrificing data quality. However, it is also apparent that the X-ray beam still required attenuation to avoid non-linearities in the detector response. Above an attenuation of the beam of 0.6% for the PILATUS3 X we found the high-intensity reflections to be systematically too low, whereas that boundary is at least 5% for the EIGER2 X. This was to some extent caused by the choice of sample which was larger than the intended sample size at SINCRYS and additionally a strong X-ray scatterer. For many of the real samples at SINCRYS it is anticipated the E2 detector will allow the operators to utilize the full flux of

the beam.

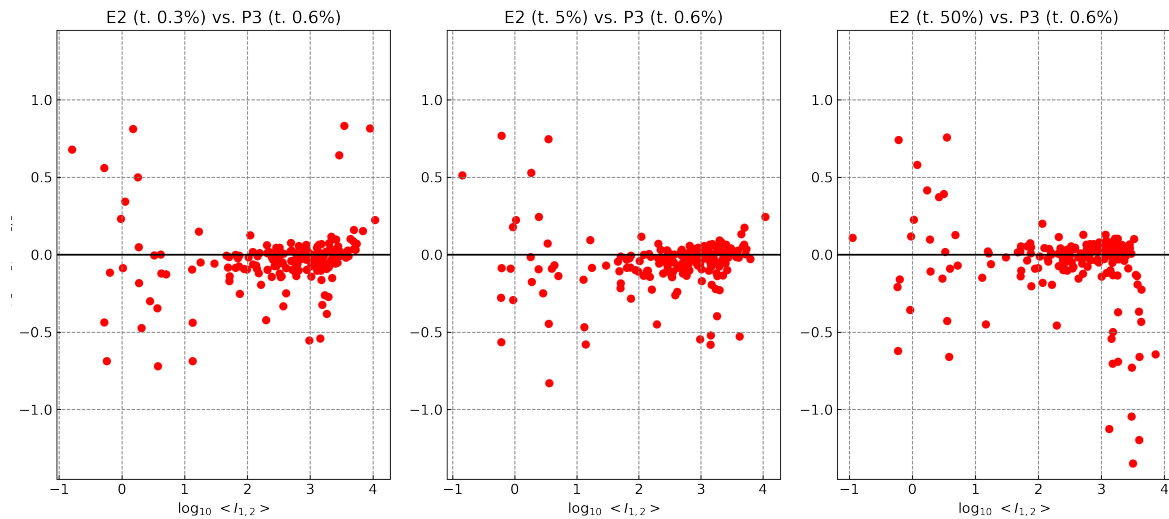


Figure 25: The \log_{10} of the intensities for a set of hkl reflections plotted against the difference over the mean with a fixed transmission for the PILATUS3 X detector, but varying transmission for the EIGER2 X detector. The figure titles show the beam transmission (t.) after attenuation in the parentheses.

3.4 Detector positioning system

To increase the observable section of reciprocal space by the detector system, it is necessary to move the detector to multiple positions. For routine structures a common position can be identified to increase the throughput, however, to not limit the capabilities of the station the detector should be able to circle around the sample to some degree. This will substantially increase the maximum achievable resolution, enable techniques such as the accurate characterisation of the charge density or the diffuse scattering of a sample. The most common solution is a 2-Theta arm to carry the detector around the sample position. Exemplary, the chemical crystallography beamline P24 at PETRA III is given here. It is built with two experimental hutches: EH1 (P24.2) with a Kappa-geometry that allows detector mounts up to 30 kg and EH2 is installed with a four circle diffractometer with a Eulerian cradle.²¹ Both diffractometers have been constructed by HUBER.

Table 14: Technical data of KR 50 R2100

Maximum Reach	[mm]	2101
Rated payload	[kg]	50
Pose repeatability	[mm]	± 0.05
Number of axes		6
Footprint	[mm ²]	603 \times 480
Weight	[kg]	533

By installing the detector on an industrial-scale robot arm, a higher flexibility is achieved

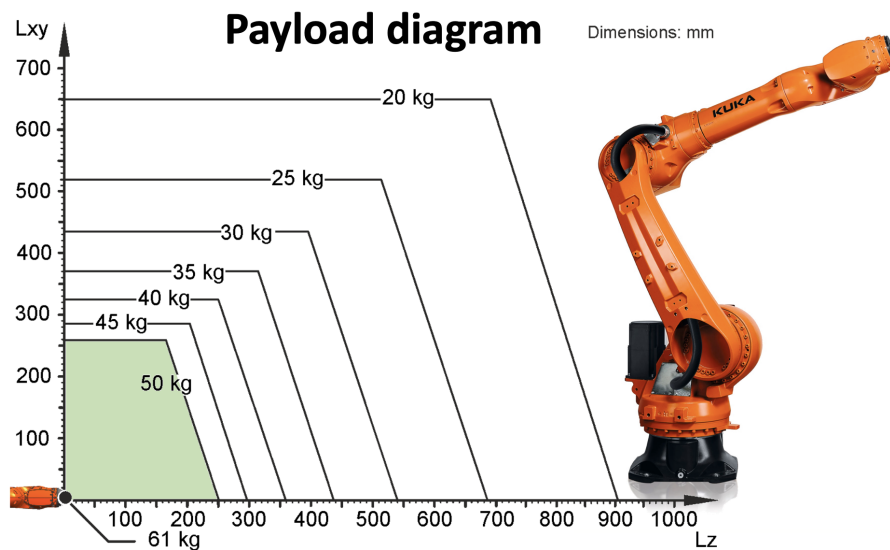


Figure 26: Payload diagram of the KUKA KR 50 R2100 robot, currently anticipated as detector mounting and positioning device.

while still retaining a high repeatability and accuracy (see Table 14). Industrial robots are designed and widely employed for tasks that are repetitive and autonomous, such as pick-and-place or welding applications. In recent years, several beamlines at synchrotron and free electron laser facilities have opted for robot arms as detector positioning systems. These include NanoMAX at MAX IV,²² MXF at LCLS,²³ DIAD K11 at Diamond Light Source,^{24,25} and NANOSCOPIUM/CRISTAL at SOLEIL.²⁶

The main concerns with employing a robot arm as a detector positioning system lies with the mechanical stability and positioning repeatability. Recently, the dual imaging and diffraction (DIAD) beamline K11 at Diamond Light Source recently reported in detail their experience with a YASKAWA robot arm for mounting a PILATUS3 X CdTe 2M detector.²⁴ The PILATUS3 detector itself weighs 49 kg, but with mounting provision and cables it comes in at a total of 139 kg. The physical dimensions of the PILATUS3 X 1M CdTe and EIGER2 X 4M CdTe detectors are listed in Table 13.

The requirement for the detector position system should be within about 1 pixel. The beam focus and divergence is slightly better in the vertical direction when compared to the horizontal direction, but within this application very small. An EIGER-pixel has a $75 \times 75 \mu\text{m}^2$ size and assuming a sample-to-detector distance of 70 mm, a half-pixel shift would translate to $0.0307^\circ = 0.54 \text{ mrad}$ (see Figure 27). The pose repeatability lies in the same region, e.g. $\pm 0.2 \text{ mm}$ for the YASKAWA MH225 as employed by the DIAD beamline, or $\pm 0.05 \text{ mm}$ for the KUKA KR50 R2100 robot with a somewhat lower payload design (shown in Figure 26) when compared to the YASKAWA model.

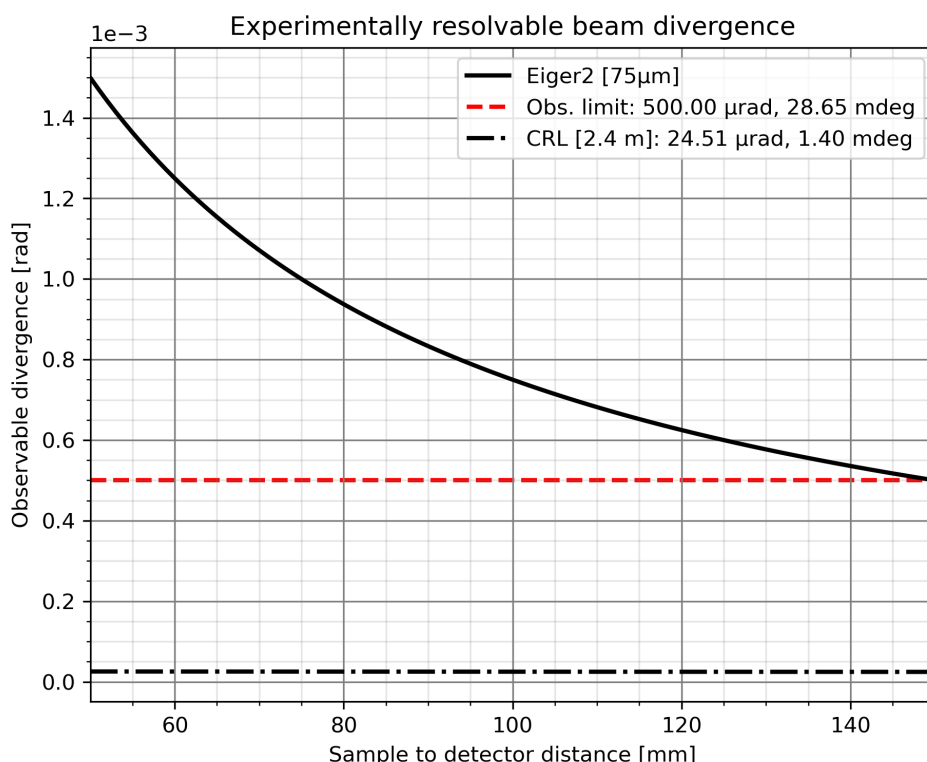


Figure 27: Resolvable divergence of the scattered beam at different sample to detector distances.

3.5 Automation and Sample Handling

Automatised crystal mounting and centring, full data collection and an overall high throughput are central pieces to the long-term vision of SINCRYS. Users should have the ability to contact the beamline staff and pay for services from mailing in a sample (see SCS, section 4). In other cases for more demanding experiments, the user might have an interest in being present for the experiment itself, or require acquisition strategies that go beyond the norm thus taking benefit from presence. However, not all aspects have to be covered right from the start. For example, upgrades such as on-axis cameras for straight-forward sample alignment or a sample changer robot are perfectly suitable future additions.

A sample changer robotic system is just mentioned here, as it is low priority at this stage. However, it is foreseen to become a requirement in 2026 - 2027 at the later stages of the beamline. The list of features necessary to help SINCRYS operate is short and only involves a sample bank, magnetic qr-coded loop-holders and a system to mount the crystals. The majority of the samples studied at SINCRYS will not require storage at cryogenic temperatures keeping the costs low.

3.6 Hutches and Infrastructure

The floor plan for DanMAX is depicted in Figure 1,¹ and was built with ample space in mind. The personnel safety system (PSS) for EH2 (SINCRYS) operates independently from DanMAX with the main branch beam passing through a shielded beampipe. Currently, however, there is no dedicated control room for SINCRYS. Since the beamlines will operate simultaneously, a new control room must be established when SINCRYS is built. The existing meeting room was designed as a multipurpose room with the necessary infrastructure for SINCRYS in mind. The DanMAX control room currently fits 3 PC stations and seats 4-6 persons. The relatively less demanding experiments (in terms of man power) warrants a smaller control room for SINCRYS. This rearrangement will be planned in detail during the procurement phase and in close collaboration with DanMAX.

Electronics racks are already established behind EH2 and in a closed room at the side of the existing control room.

Lines for liquid nitrogen (LN2) must be established for SINCRYS at the experimental station, as it is not viable to transport Dewar bottles regularly.

4 Scandinavian Crystallography Service

The general applicability and accessibility of SINCRYs will be maximized by launching a Scandinavian Crystallography Service (SCS) to be used by industry and researchers e.g. within organic chemistry, medicinal chemistry, materials science, polymer chemistry, and biochemistry. Worldwide, the synthesis groups within these fields provide the intellectual foundations for much of the chemical industry and they are critically dependent on accurate 3D structure information. By integration of SINCRYs into the MAX IV infrastructure, seamless access for researchers all over Scandinavia is assured. The principal investigators have world-leading expertise within small molecule crystallography, which will guarantee the construction of an absolute state-of-the-art facility, and the large direct community represented by 79 independent research groups supporting the application testifies to the extremely broad appeal of the infrastructure.

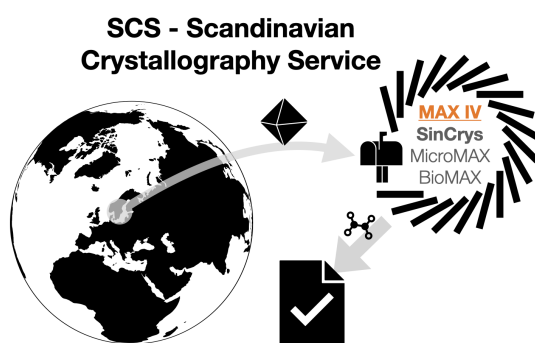


Figure 28: Sketch of the workflow of the Scandinavian Crystallography Service (SCS).

Chemical synthesis groups all over Scandinavia, both in industry and academia, rely on 3D atomic structure information from single crystal X-ray diffraction. A portal for service crystallography will work on a “mail-in” basis as well as direct interaction between the SCS scientists and local research group. SCS scientists will travel to local research communities to actively discuss and collect samples. Experiments can be ordered online by directly transferring required sample information to the control system database and generating shipping labels directly on the webpage. Once the service enters routine operation we expect service structures to be available within two weeks though dependent on the beamline schedule and sample complexity. Services will span from measurements of data (for experienced crystallographers) to full publication ready analysis.

To ensure the best possible start to this service, an application was submitted to the call for Research Infrastructure – Large equipment and facilities of the Novo Nordisk Fonden (NNF) in January, 2023. The application includes funding for a 5-year full-time Technician with the beginning of 2024. The project will begin early, before SINCRYs takes first light in the experimental hutch, by utilizing available time at the existing BioMAX and MicroMAX beamlines. By starting early, it ensures SINCRYs will hit the ground running, once the beamline enters commissioning and user operation.

5 Project Timeline & Budget

5.1 Budget

The project was officially kicked off in January 2022 with the successful hire of Assistant Research Professor Lennard Krause (5 year position with tenure track) and Postdoc Martin Roelsgaard (2 year position). The project has a 5-year timeline from the onset, and has been shifted according to the originally planned start in the fall of 2021. The budget is itemized in Table 15.

Table 15: SINCRYS budget.

Item	Budget [MDKK]
X-ray optics	4.40
Vacuum and beam transport	3.10
Detector	3.50
Endstation equipment	4.60
Salaries (AU)	6.90
Shared resources at MAX IV	2.00
External consultants	0.50
TOTAL	25.00
Application budget	25.00

5.2 Installation considerations

DanMAX is in user operation, which the installation of SINCRYS should minimally impact. It is, however, not possible to avoid all collision with operation of DanMAX in particular during the early installation procedures of SINCRYS. The two main culprits are the installation of the first monochromator crystal, which needs to be inserted into the transfer pipe between the high-pass filter of DanMAX and the receiving slits of the hDCM monochromator at DanMAX.

The second large alteration of the DanMAX optical layout is the need for a new hole between the optics hutch and second experimental hutch (future SINCRYS) hutch. These operations are foreseen to be handled during general machine shutdown periods of MAX IV, to avoid harming the user program of DanMAX.

A second consequence to the existing infrastructure at DanMAX is the floor space that will be required for SINCRYS on the outboard side of the DanMAX optical train. DanMAX has been constructed with this in mind *i.e.* all electrical connections are installed on the inboard side for maintenance.

References

- (1) Jørgensen, M. R. V.; Kantor, I. *Detailed Design Report for DanMAX: Powder Diffraction Instruments*; Technical Design Report; Fotongatan 2, 224 84 Lund, Sweden: Aarhus University & MAX IV Laboratory, 2018.
- (2) Sondhauss, P. In ed. by del Rio, M. S.; Chubar, O., 2014, p 92090C, DOI: 10.1117/12.2061007.
- (3) Tanaka, T. *Journal of Synchrotron Radiation* **2021**, 28, 1267–1272, DOI: 10.1107/S1600577521004100.
- (4) Als-Nielsen, J.; Freund, A.; Grübel, G.; Linderholm, J.; Nielsen, M.; del Rio, M.; Sell-schop, J. *Nuclear Instruments and Methods in Physics Research Section B: Beam Interactions with Materials and Atoms* **1994**, 94, 306–318, DOI: 10.1016/0168-583X(94)95370-8.
- (5) Source, A. P. *Advanced Photon Source Upgrade Project - Final Design Report*; Technical Design Report; 9700 South Cass Avenue, Argonne, Illinois 60439, USA: Argonne National Laboratory, 2019.
- (6) Zhu, D. et al. *Review of Scientific Instruments* **2014**, 85, 063106, DOI: 10.1063/1.4880724.
- (7) Stoupin, S. et al. *Journal of Applied Crystallography* **2014**, 47, 1329–1336, DOI: 10.1107/S1600576714013028, <https://scripts.iucr.org/cgi-bin/paper?S1600576714013028>.
- (8) Bowler, M. W. et al. *Journal of Synchrotron Radiation* **2015**, 22, 1540–1547, DOI: 10.1107/S1600577515016604, <https://scripts.iucr.org/cgi-bin/paper?S1600577515016604>.
- (9) Von Stetten, D. et al. *Journal of Synchrotron Radiation* **2020**, 27, 844–851, DOI: 10.1107/S1600577520004002, <https://scripts.iucr.org/cgi-bin/paper?S1600577520004002>.
- (10) *Journal of Synchrotron Radiation* **2015**, 22, 675–687, DOI: 10.1107/S1600577515002222.
- (11) Ursby, T.; Unge, J.; Appio, R.; Logan, D. T.; Fredslund, F.; Svensson, C.; Larsson, K.; Labrador, A.; Thunnissen, M. M. G. M. *Journal of Synchrotron Radiation* **2013**, 20, 648–653, DOI: 10.1107/S0909049513011734, <https://scripts.iucr.org/cgi-bin/paper?S0909049513011734>.
- (12) Tsusaka, Y.; Yokoyama, K.; Takeda, S.; Takai, K.; Kagoshima, Y.; Matsui, J. *Nuclear Instruments and Methods in Physics Research Section A: Accelerators, Spectrometers, Detectors and Associated Equipment* **2001**, 467-468, 670–673, DOI: 10.1016/S0168-9002(01)00440-5, <https://linkinghub.elsevier.com/retrieve/pii/S0168900201004405>.
- (13) Shvyd'ko, Y.; Stoupin, S.; Blank, V.; Terentyev, S. *Nature Photonics* **2011**, 5, 539–542, DOI: 10.1038/nphoton.2011.197.
- (14) Chumakov, A.; Rüffer, R.; Leupold, O.; Celse, J.-P.; Martel, K.; Rossat, M.; Lee, W.-K. *Journal of Synchrotron Radiation* **2004**, 11, 132–141, DOI: 10.1107/S0909049503026785, <https://scripts.iucr.org/cgi-bin/paper?S0909049503026785>.

- (15) Burns, R. C.; Chumakov, A. I.; Connell, S. H.; Dube, D.; Godfried, H. P.; Hansen, J. O.; Härtwig, J.; Hoszowska, J.; Masiello, F.; Mkhonza, L.; Rebak, M.; Rommevaux, A.; Setshedi, R.; Van Vaerenbergh, P. *Journal of Physics: Condensed Matter* **2009**, *21*, 364224, DOI: 10.1088/0953-8984/21/36/364224, <https://iopscience.iop.org/article/10.1088/0953-8984/21/36/364224>.
- (16) Stoupin, S.; Antipov, S.; Butler, J. E.; Kolyadin, A. V.; Katrusha, A. *Journal of Synchrotron Radiation* **2016**, *23*, 1118–1123, DOI: 10.1107/S1600577516011796, <https://scripts.iucr.org/cgi-bin/paper?S1600577516011796>.
- (17) Serebrennikov, D.; Clementyev, E.; Semenov, A.; Snigirev, A. *Journal of Synchrotron Radiation* **2016**, *23*, 1315–1322, DOI: 10.1107/S1600577516014508, <https://scripts.iucr.org/cgi-bin/paper?S1600577516014508>.
- (18) Celestre, R.; Antipov, S.; Gomez, E.; Zinn, T.; Barrett, R.; Roth, T. *Journal of Synchrotron Radiation* **2022**, *29*, 629–643, DOI: 10.1107/S1600577522001795, <https://scripts.iucr.org/cgi-bin/paper?S1600577522001795>.
- (19) Krause, L.; Tolborg, K.; Grønbech, T. B. E.; Sugimoto, K.; Iversen, B. B.; Overgaard, J. *Journal of Applied Crystallography* **2020**, *53*, 635–649, DOI: 10.1107/S1600576720003775.
- (20) Pennicard, D.; Graafsma, H. *Journal of Instrumentation* **2011**, *6*, P06007–P06007, DOI: 10.1088/1748-0221/6/06/P06007, <https://iopscience.iop.org/article/10.1088/1748-0221/6/06/P06007>.
- (21) Tolkiehn, M.; Schulz-Ritter, H.; Drube, W.; Paulmann, C.; Berghäuser, A.; Ropers, D. *Beamline P24 - Chemical Crystallography: Technical Design Report*; Technical Design Report; Notkestr. 85, 22607 Hamburg, Germany: PETRA III, Deustches Elektronen-Synchrotron, 2014.
- (22) Johansson, U. et al. *Journal of Synchrotron Radiation* **2021**, *28*, 1935–1947, DOI: 10.1107/S1600577521008213, <https://scripts.iucr.org/cgi-bin/paper?S1600577521008213>.
- (23) Sierra, R. G. et al. *Journal of Synchrotron Radiation* **2019**, *26*, 346–357, DOI: 10.1107/S1600577519001577, <http://scripts.iucr.org/cgi-bin/paper?S1600577519001577>.
- (24) Reinhart, C.; Drakopoulos, M.; Charlesworth, C. M.; James, A.; Patel, H.; Tutthill, P.; Crivelli, D.; Deyhle, H.; Ahmed, S. I. *Journal of Synchrotron Radiation* **2022**, *29*, 1004–1013, DOI: 10.1107/S1600577522006300, <https://scripts.iucr.org/cgi-bin/paper?S1600577522006300>.
- (25) Reinhart, C. et al. *Journal of Synchrotron Radiation* **2021**, *28*, 1985–1995, DOI: 10.1107/S1600577521009875, <https://scripts.iucr.org/cgi-bin/paper?S1600577521009875>.
- (26) Abiven, Y.-M.; Bouvel, S.; Bucaille, T.; Chavas, L.; Elkaim, E.; Gourhant, P.; Liatimi, Y.; Medjoubi, K.; Zéphir, S. P.-J.; Pilliaud, B.; Pinty, V.; Somogyi, A.; Thiam, F. In 2020, DOI: 10.18429/JACoW-ICALEPCS2019-MOPHA001.
- (27) Rutkowski, J.; Brzezinski, B. *BioMed Research International* **2013**, *2013*, 1–31, DOI: 10.1155/2013/162513.
- (28) II, D. A. K.; Meujo, D. A.; Hamann, M. T. *Expert Opinion on Drug Discovery* **2009**, *4*, 109–146, DOI: 10.1517/17460440802661443.

- (29) Liu, H.; Lin, S.; Jacobsen, K. M.; Poulsen, T. B. *Angewandte Chemie International Edition* **2019**, *58*, 13630–13642, DOI: [10.1002/anie.201812982](https://doi.org/10.1002/anie.201812982).
- (30) Lin, S.; Liu, H.; Svenningsen, E. B.; Wollesen, M.; Jacobsen, K. M.; Andersen, F. D.; Moyano-Villameriel, J.; Pedersen, C. N.; Nørby, P.; Tørring, T.; Poulsen, T. B. *Nature Chemistry* **2021**, *13*, 47–55, DOI: [10.1038/s41557-020-00601-1](https://doi.org/10.1038/s41557-020-00601-1).
- (31) Kellett, A.; Molphy, Z.; McKee, V.; Slator, C. In *Metal-based Anticancer Agents*, 2019, pp 91–119, DOI: [10.1039/9781788016452-00091](https://doi.org/10.1039/9781788016452-00091).
- (32) Slator, C.; Barron, N.; Howe, O.; Kellett, A. *ACS Chemical Biology* **2016**, *11*, 159–171, DOI: [10.1021/acschembio.5b00513](https://doi.org/10.1021/acschembio.5b00513).
- (33) Slator, C.; Molphy, Z.; McKee, V.; Long, C.; Brown, T.; Kellett, A. *Nucleic Acids Research* **2018**, *46*, 2733–2750, DOI: [10.1093/nar/gky105](https://doi.org/10.1093/nar/gky105).
- (34) Southon, P. D.; Price, D. J.; Nielsen, P. K.; McKenzie, C. J.; Kepert, C. J. *Journal of the American Chemical Society* **2011**, *133*, 10885–10891, DOI: [10.1021/ja202228v](https://doi.org/10.1021/ja202228v).
- (35) Lennartson, A.; Southon, P.; Sciortino, N. F.; Kepert, C. J.; Frandsen, C.; Mørup, S.; Piligkos, S.; McKenzie, C. J. *Chemistry – A European Journal* **2015**, *21*, 16066–16072, DOI: [10.1002/chem.201502547](https://doi.org/10.1002/chem.201502547).
- (36) Wegeberg, C.; Nielsen, D.; Mossin, S.; Abrahams, B. F.; McKee, V.; McKenzie, C. J. *Australian Journal of Chemistry* **2019**, *72*, 817, DOI: [10.1071/CH19264](https://doi.org/10.1071/CH19264).
- (37) Møller, M. S.; Haag, A.; McKee, V.; McKenzie, C. J. *Chemical Communications* **2019**, *55*, 10551–10554, DOI: [10.1039/C9CC05315H](https://doi.org/10.1039/C9CC05315H).
- (38) De Sousa, D. P.; Bigelow, J. O.; Sundberg, J.; Que, L.; McKenzie, C. J. *Chemical Communications* **2015**, *51*, 2802–2805, DOI: [10.1039/C4CC08785B](https://doi.org/10.1039/C4CC08785B).
- (39) Aree, T.; Bürgi, H.-B.; Chernyshov, D.; Törnroos, K. W. *The Journal of Physical Chemistry A* **2014**, *118*, 9951–9959, DOI: [10.1021/jp506659c](https://doi.org/10.1021/jp506659c).
- (40) Hoser, A. A.; Madsen, A. Ø. *Acta Crystallographica Section A Foundations and Advances* **2017**, *73*, 102–114, DOI: [10.1107/S2053273316018994](https://doi.org/10.1107/S2053273316018994).
- (41) Kofoed, P. M.; Hoser, A. A.; Diness, F.; Capelli, S. C.; Madsen, A. Ø. *IUCrJ* **2019**, *6*, 558–571, DOI: [10.1107/S2052252519003014](https://doi.org/10.1107/S2052252519003014).
- (42) Sovago, I.; Hoser, A. A.; Madsen, A. Ø. *Acta Crystallographica Section A Foundations and Advances* **2020**, *76*, 32–44, DOI: [10.1107/S205327331901355X](https://doi.org/10.1107/S205327331901355X).
- (43) Wehinger, B.; Mirone, A.; Krisch, M.; Bosak, A. *Physical Review Letters* **2017**, *118*, 035502, DOI: [10.1103/PhysRevLett.118.035502](https://doi.org/10.1103/PhysRevLett.118.035502).
- (44) Desiraju, G. R. *Nature* **2001**, *412*, 397–400, DOI: [10.1038/35086640](https://doi.org/10.1038/35086640).
- (45) Seddon, A. M.; Casey, D.; Law, R. V.; Gee, A.; Templer, R. H.; Ces, O. *Chemical Society Reviews* **2009**, *38*, 2509, DOI: [10.1039/b813853m](https://doi.org/10.1039/b813853m).
- (46) Muthukumar, M.; Ober, C. K.; Thomas, E. L. *Science* **1997**, *277*, 1225–1232, DOI: [10.1126/science.277.5330.1225](https://doi.org/10.1126/science.277.5330.1225).
- (47) Stupp, S. I.; LeBonheur, V.; Walker, K.; Li, L. S.; Huggins, K. E.; Keser, M.; Amstutz, A. *Science* **1997**, *276*, 384–389, DOI: [10.1126/science.276.5311.384](https://doi.org/10.1126/science.276.5311.384).

- (48) Lennartson, A.; McKenzie, C. J. *Angewandte Chemie International Edition* **2012**, *51*, 6767–6770, DOI: [10.1002/anie.201202487](https://doi.org/10.1002/anie.201202487).
- (49) De Sousa, D. P.; Wegeberg, C.; Vad, M. S.; Mørup, S.; Frandsen, C.; Donald, W. A.; McKenzie, C. J. *Chemistry - A European Journal* **2016**, *22*, 3810–3820, DOI: [10.1002/chem.201503112](https://doi.org/10.1002/chem.201503112).
- (50) Tolborg, K.; Iversen, B. B. *Chemistry – A European Journal* **2019**, *25*, 15010–15029, DOI: [10.1002/chem.201903087](https://doi.org/10.1002/chem.201903087).
- (51) Shi, M. W.; Thomas, S. P.; Hathwar, V. R.; Edwards, A. J.; Piltz, R. O.; Jayatilaka, D.; Koutsantonis, G. A.; Overgaard, J.; Nishibori, E.; Iversen, B. B.; Spackman, M. A. *Journal of the American Chemical Society* **2019**, *141*, 3965–3976, DOI: [10.1021/jacs.8b12927](https://doi.org/10.1021/jacs.8b12927).
- (52) Clausen, H. F.; Jørgensen, M. R. V.; Cenedese, S.; Schmøkel, M. S.; Christensen, M.; Chen, Y.-S.; Koutsantonis, G.; Overgaard, J.; Spackman, M. A.; Iversen, B. B. *Chemistry - A European Journal* **2014**, *20*, 8089–8098, DOI: [10.1002/chem.201400129](https://doi.org/10.1002/chem.201400129).
- (53) Walker, J.; Miranti, R.; Skjærvø, S. L.; Rojac, T.; Grande, T.; Einarsrud, M.-A. *Journal of Materials Chemistry C* **2020**, *8*, 3206–3216, DOI: [10.1039/C9TC06918F](https://doi.org/10.1039/C9TC06918F).
- (54) Rude, L. H.; Corno, M.; Ugliengo, P.; Baricco, M.; Lee, Y.-S.; Cho, Y. W.; Besenbacher, F.; Overgaard, J.; Jensen, T. R. *The Journal of Physical Chemistry C* **2012**, *116*, 20239–20245, DOI: [10.1021/jp306665a](https://doi.org/10.1021/jp306665a).
- (55) Møller, K. T.; Paskevicius, M.; Andreasen, J. G.; Lee, J.; Chen-Tan, N.; Overgaard, J.; Payandeh, S.; Silvester, D. S.; Buckley, C. E.; Jensen, T. R. *Chemical Communications* **2019**, *55*, 3410–3413, DOI: [10.1039/C9CC00187E](https://doi.org/10.1039/C9CC00187E).
- (56) Weber, T.; Simonov, A. *Zeitschrift für Kristallographie* **2012**, *227*, 238–247, DOI: [10.1524/zkri.2012.1504](https://doi.org/10.1524/zkri.2012.1504).
- (57) Roth, N.; Iversen, B. B. *Acta Crystallographica Section A Foundations and Advances* **2019**, *75*, 465–473, DOI: [10.1107/S2053273319004820](https://doi.org/10.1107/S2053273319004820).
- (58) Kageyama, H.; Hayashi, K.; Maeda, K.; Attfield, J. P.; Hiroi, Z.; Rondinelli, J. M.; Poeppelmeier, K. R. *Nature Communications* **2018**, *9*, 772, DOI: [10.1038/s41467-018-02838-4](https://doi.org/10.1038/s41467-018-02838-4).
- (59) Ma, Z.; Jaworski, A.; George, J.; Rokicinska, A.; Thersleff, T.; Budnyak, T. M.; Hautier, G.; Pell, A. J.; Dronkowski, R.; Kuśtrowski, P.; Slabon, A. *The Journal of Physical Chemistry C* **2020**, *124*, 152–160, DOI: [10.1021/acs.jpcc.9b09838](https://doi.org/10.1021/acs.jpcc.9b09838).
- (60) Davi, M.; Schrader, F.; Scholz, T.; Ma, Z.; Rokicinska, A.; Dronkowski, R.; Kustrowski, P.; Slabon, A. *ACS Applied Nano Materials* **2018**, *1*, 869–876, DOI: [10.1021/acsanm.7b00269](https://doi.org/10.1021/acsanm.7b00269).
- (61) Ma, Z.; Thersleff, T.; Görne, A. L.; Cordes, N.; Liu, Y.; Jakobi, S.; Rokicinska, A.; Schichtl, Z. G.; Coridan, R. H.; Kustrowski, P.; Schnick, W.; Dronkowski, R.; Slabon, A. *ACS Applied Materials & Interfaces* **2019**, *11*, 19077–19086, DOI: [10.1021/acsami.9b02483](https://doi.org/10.1021/acsami.9b02483).

- (62) Davi, M.; Drichel, A.; Mann, M.; Scholz, T.; Schrader, F.; Rokicinska, A.; Kustrowski, P.; Dronkowski, R.; Slabon, A. *The Journal of Physical Chemistry C* **2017**, *121*, 26265–26274, DOI: [10.1021/acs.jpcc.7b10220](https://doi.org/10.1021/acs.jpcc.7b10220).
- (63) Lu, C.; Jothi, P. R.; Thersleff, T.; Budnyak, T. M.; Rokicinska, A.; Yubuta, K.; Dronkowski, R.; Kuśkowski, P.; Fokwa, B. P. T.; Slabon, A. *Nanoscale* **2020**, *12*, 3121–3128, DOI: [10.1039/C9NR09818F](https://doi.org/10.1039/C9NR09818F).
- (64) Zhang, N.; Li, L.; Shao, Q.; Zhu, T.; Huang, X.; Xiao, X. *ACS Applied Energy Materials* **2019**, *2*, 8394–8398, DOI: [10.1021/acsaem.9b01961](https://doi.org/10.1021/acsaem.9b01961).
- (65) Shi, Y.; Assoud, A.; Ponou, S.; Lidin, S.; Kleinke, H. *Journal of the American Chemical Society* **2018**, *140*, 8578–8585, DOI: [10.1021/jacs.8b04639](https://doi.org/10.1021/jacs.8b04639).
- (66) Abakumov, A. M.; Rossell, M. D.; Gutnikova, O. Y.; Drozhzhin, O. A.; Leonova, L. S.; Dobrovolsky, Y. A.; Istomin, S. Y.; Tendeloo, G. V.; Antipov, E. V. *Chemistry of Materials* **2008**, *20*, 4457–4467, DOI: [10.1021/cm8004216](https://doi.org/10.1021/cm8004216).
- (67) Van Smaalen, S. *Acta Crystallographica Section A Foundations of Crystallography* **2005**, *61*, 51–61, DOI: [10.1107/S0108767304025437](https://doi.org/10.1107/S0108767304025437).
- (68) Takakura, H.; Gómez, C. P.; Yamamoto, A.; Boissieu, M. D.; Tsai, A. P. *Nature Materials* **2007**, *6*, 58–63, DOI: [10.1038/nmat1799](https://doi.org/10.1038/nmat1799).
- (69) Lidin, S.; Folkers, L. C. *Accounts of Chemical Research* **2018**, *51*, 223–229, DOI: [10.1021/acs.accounts.7b00508](https://doi.org/10.1021/acs.accounts.7b00508).
- (70) *Acta Crystallographica Section A Foundations of Crystallography* **1992**, *48*, 922–946, DOI: [10.1107/S0108767392008328](https://doi.org/10.1107/S0108767392008328).
- (71) Pedersen, K. S.; Bendix, J.; Clérac, R. *Chem. Commun.* **2014**, *50*, 4396–4415, DOI: [10.1039/C4CC00339J](https://doi.org/10.1039/C4CC00339J).
- (72) Pedersen, K. S.; Woodruff, D. N.; Bendix, J.; Clérac, R. In *Lanthanides and Actinides in Molecular Magnetism*; Wiley-VCH Verlag GmbH & Co. KGaA: 2015, pp 125–152, DOI: [10.1002/9783527673476.ch5](https://doi.org/10.1002/9783527673476.ch5).
- (73) Pedersen, K. S.; Dreiser, J.; Weihe, H.; Sibille, R.; Johannessen, H. V.; Sørensen, M. A.; Nielsen, B. E.; Sigrist, M.; Mutka, H.; Rols, S.; Bendix, J.; Piligkos, S. *Inorganic Chemistry* **2015**, *54*, 7600–7606, DOI: [10.1021/acs.inorgchem.5b01209](https://doi.org/10.1021/acs.inorgchem.5b01209).
- (74) Chhowalla, M.; Jena, D.; Zhang, H. *Nature Reviews Materials* **2016**, *1*, 16052, DOI: [10.1038/natrevmats.2016.52](https://doi.org/10.1038/natrevmats.2016.52).
- (75) Lin, X.; Yang, W.; Wang, K. L.; Zhao, W. *Nature Electronics* **2019**, *2*, 274–283, DOI: [10.1038/s41928-019-0273-7](https://doi.org/10.1038/s41928-019-0273-7).
- (76) Pedersen, K. S. et al. *Nature Chemistry* **2018**, *10*, 1056–1061, DOI: [10.1038/s41557-018-0107-7](https://doi.org/10.1038/s41557-018-0107-7).
- (77) Refn, V. E.; Kubus, M.; Mossin, S.; Larsen, R. W.; Pedersen, K. S. *ACS Omega* **2020**, *5*, 3462–3466, DOI: [10.1021/acsomega.9b03727](https://doi.org/10.1021/acsomega.9b03727).
- (78) Vinum, M. G.; Voigt, L.; Bell, C.; Mihrin, D.; Larsen, R. W.; Clark, K. M.; Pedersen, K. S. *Chemistry – A European Journal* **2020**, *26*, 2143–2147, DOI: [10.1002/chem.201904899](https://doi.org/10.1002/chem.201904899).

- (79) Olsen, L. A.; Balić-Žunić, T.; Makovicky, E. *Inorganic Chemistry* **2008**, *47*, 6756–6762, DOI: [10.1021/ic800380p](https://doi.org/10.1021/ic800380p).
- (80) Olsen, L. A.; Friese, K.; Makovicky, E.; Balić-Žunić, T.; Morgenroth, W.; Grzechnik, A. *Physics and Chemistry of Minerals* **2011**, *38*, 1–10, DOI: [10.1007/s00269-010-0376-1](https://doi.org/10.1007/s00269-010-0376-1).
- (81) Balic-Zunic, T.; Piazolo, S.; Katerinopoulou, A.; Schmitt, J. H. *American Mineralogist* **2013**, *98*, 41–52, DOI: [10.2138/am.2013.4124](https://doi.org/10.2138/am.2013.4124).

A Appendix A

A.1 Science cases and SINCRYS Consortium

The SINCRYS project consists of a consortium of 79 independent research groups and industry from all over Scandinavia that support the project and will positively benefit from the instrument. The individual groups span many scientific disciplines but they share the need for accessible synchrotron single-crystal X-ray diffraction around the corner. Once the capabilities of the SINCRYS beamline become generally known, it is also anticipated that new user groups will enter the community.

The following section is composed of science cases representative for the SINCRYS backers, referring to the listed references.

Life science

STRUCTURE-ACTIVITY RELATIONS OF CARBOXYL POLYETHER IONOPHORES (CPIs). The CPIs form a class of >150 highly complex natural products with interesting antibiotic activities,²⁷ although their biological role still remains obscure. Since CPIs equilibrate ion-gradients across biological membranes, they are thought to be unspecific and pleiotropic. This, however, contrasts with their antibiotic potency and their effects on mammalian cells both of which display significant variability.²⁸ In order to study the origin of the biological functions of CPIs, structure-activity relations across several different activities (in vitro and in cellular systems) must be compared, but accessing the structural diversity is extremely challenging due to their complexity.²⁹ In an ERC consolidator project, the Poulsen group will develop new synthesis strategies,³⁰ and although most natural CPIs can be crystallized as cation-complexes, the project will focus on variants that strongly perturb coordination geometries. These are difficult to crystallize making microcrystallography essential.

DNA-BINDING CANCER THERANOSTICS. Triplex forming oligonucleotide (TFO) hybrids for anchoring radioactive metal complexes to DNA^{31–33} have immense potential for precision targeting TFOs in cancer cells for the purposes of diagnostic scanning (PET, SPECT) and critically precision radiotherapy. This research is challenged by micron-sized crystals. SINCRYS will permit McKenzie, McKee and Wengel to carry out structural analysis of these hybrids, and the crystal structures of these supermolecules will have significant general impact, since very few structures of TFOs exist.

MOLECULAR CATALYSTS AND IN-CRYSTAL REACTIONS. Metal-organic compounds, including MOFs, can chemisorb inert gases and vapours.^{34–36} By exploiting this property the McKenzie group is developing new methodologies for catalysing solvent-free reactions by crystalline state-entrapped molecular catalysts. The mechanisms involved can be likened to those employed by a myriad of redox metalloenzymes for selectively binding and metabolizing the gaseous building block of life (O₂, N₂, H₂, H₂O, CO₂, CH₄). New materials will contain metallic active sites for the binding and selective activation of gases, and furnish the migration of substrates and products in and out of the solid materials.^{37,38} These complex molecular catalysts often are difficult to crystallize making SINCRYS essential. In general, new methods for exploiting gases will open up for energy-efficient and green synthetic chemistry as O₂ e.g. can replace toxic oxidants in the production of fine chemicals.

LATTICE DYNAMICS OF PHARMACEUTICAL CRYSTALS. The thermodynamic, kinetic and mechanical properties of molecular crystals are, in a pharmaceutical context, crucial for the design and manufacturing of solid-state dosage forms: More than 50% of all drugs are produced in a crystalline form, most of them as tablets. The crystal properties are not only governed by the static average structure, but also by the dynamics of the crystal lattice. Single-crystal X-ray diffraction can be used to rationalize the thermodynamic relationships between polymorphic molecular crystals,^{39–42} and weak thermal diffuse scattering measured from single crystals can give accurate elastic properties of crystals.⁴³ The Madsen group will use these approaches to develop a more rational design of crystalline pharmaceutical materials.

WEAK INTERMOLECULAR INTERACTIONS. Biological science and supramolecular chemistry are controlled by the nature of interactions between molecules.⁴⁴ The weak noncovalent interactions drive complex phenomena such as self-assembly and nucleation, ligand receptor binding or enzymatic catalysis,^{45–47} or the solid-state stabilization of reactive compounds,^{48,49} yet they are poorly understood and extremely difficult to quantify with current theoretical methods. Accurate single crystal X-ray diffraction measurements provide access to the electron density of crystals,⁵⁰ giving access to description of intermolecular interactions.^{51,52} The Iversen group will study weak intermolecular interactions in small molecular complexes to provide fundamental insight about the interplay between molecules in larger structures. A related direction explored by the Einarsrud group is plastic ferroelectric crystals, where weak interactions are also essential for properties.⁵³

Sustainable energy

HYDROGEN STORAGE AND SOLID STATE ELECTROLYTES. Hydrogen is the lightest element, and it has the highest gravimetric energy content of any substance. Hydrogen also forms the greatest variety of different chemical interactions and compounds. As an example, the structure of Zr(BH₄)₄ contains peculiar short intermolecular BH · · · HB interactions.⁵⁴ Understanding the huge diversity of hydrogen chemical interactions is essential for developing better hydrogen storage materials and solid-state electrolytes for batteries. Battery properties depend on how well the electrode structure accommodate the ions and allow ion diffusion.⁵⁵ The Jensen and Ravnsbæk groups seek detailed atomic structures to understand ion-migration pathways and phase co-existence in single particles.

THERMOELECTRIC MATERIALS can interconvert heat and electricity making it possible to harvest waste heat from engines and industrial processes. Many materials have atomic disorder as the root to their properties making it difficult to derive effective structure–property relations. Periodic ordered crystal structures give sharp Bragg peaks, whereas correlated disorder lead to diffuse scattering, which is typically three orders of magnitude weaker. Synchrotron measurements of weak diffuse scattering and has led to the birth of the 3D Pair Distribution Function (3D-PDF) method to quantify correlated disorder.⁵⁶ The Iversen group recently reported the first disordered crystal structure solved by 3D-PDF thereby launching “the crystallography of disorder”.⁵⁷ At SINCRYs measurement of diffuse scattering will give a quantitative understanding of the influence of structural disorder on transport properties.

PHOTOCATALYSTS. Mixed-anion materials (MAMs) consist of more than one anionic species in the crystal structure, such as metal oxyfluorides. MAMs have potential applications in batteries, pleochromism, photocatalysis and heterogeneous catalysis.^{58,59} Metal oxyhalides and oxynitrides are prospective materials for the photoelectrochemical synthesis of H₂,^{60,61} and

carbodiimides have recently been reported as a promising class of compounds.⁶² The Slabon group will synthesize new semiconducting MAMs with electronic bands gap below 2.4 eV in order to ensure sufficient solar light harvesting. The discovery of new MAMs will trigger investigations with respect to their application in photoelectrochemical water-splitting,⁶³ photocatalytic decomposition of organic pollutants in wastewater, and photocatalytic nitrogen reduction.⁶⁴

Materials science

QUASICRYSTALS AND MODULATED STRUCTURES. Properties of functional inorganic materials are often determined by perturbations of the long-range order.⁶⁵ Such structural modulations can result from agglomeration ordering of defects,⁶⁶ or they can be purely quantum in nature, as in charge-wave instabilities or Peierls distortions.⁶⁷ The satellite reflections that accompany modulated structures are typically very weak making detailed analysis challenging. For quasicrystals all high quality structures to date were solved from synchrotron data.^{68,69} The discovery of quasicrystals has had a profound impact on crystallography and even resulted in the re-definition of a crystal.⁷⁰ The Mudring, Gomez, Lidin and Häusserman groups are world-leading in the field of aperiodic structures and SINCRYs will strongly enhance their experimental capabilities.⁶⁸

MOLECULAR MAGNETS. Structure-function relationships are central in the development molecular magnets for quantum information storage and processing.^{71,72} Without single-crystal structure information property optimization is impossible. Many mechanisms are operational in the relaxation processes, which limits the properties of molecular magnets. Crystal lattice vibrations are particularly important making engineering of the phonon spectrum imperative.⁷³ Screening of large ensembles of crystals of a single material for crystal quality, and systematic comparison of structures for arrays of chemically modified systems will be important in this context. The Bendix group will use SINCRYs to determine packing patters for molecular magnets and correlate these with phonon spectra determined by THZ and neutron spectroscopies. Another key direction is single molecule magnets (SMMs), which is pursued by the Overgaard group. Here individual molecules exhibit magnetic bi-stability in a given temperature regime, and the functionality is governed by the molecular structure. SMMs often are only available as microcrystals, making SINCRYs ideal to achieve new progress.

2D METAL-ORGANIC MATERIALS. 2D materials such as graphene and transition metal disulfides have extraordinary properties central to emerging technologies like molecular-scale transistors⁷⁴ and spintronics.⁷⁵ However, the simple chemical nature of existing 2D materials leaves little possibility for property optimization. The Pedersen group designs novel layered materials^{76,77} using synthetic principles borrowed from molecule-based chemistry.⁷⁸ The molecular engineering of inorganic and organic modules leads to almost endless possibilities for tailoring electronic, magnetic, and electrochemical properties. However, the complexity of these materials and the difficulty of growing large single-crystals makes synchrotron studies necessary. Pedersen will study magnetic conductive layered materials to understand the relationship between the molecular-level structure and the ensuing physical properties in 2D materials.

Crystallography

HIGH-PRESSURE STUDIES. External pressure modifies material properties making design of new materials possible. Pressure affects the bonding of the atoms in crystals and its relationships with the electronic and magnetic properties. Single crystal X-ray diffraction under pressure can be measured using diamond anvil cells, but the small sample volume means that an intense and focused X-ray source is required. Overgaard will use pressure to modify the distribution of coordinating ligands around a central metal atom in single molecule magnets to understand their influence of the magnetic properties. Bremholm will use pressure to study phase transitions and electronic properties of complex inorganic materials. An unexplored field is to study how the rate of pressure change can lead to different crystal polymorphs e.g. in pharmaceutical compounds.

MINERALOGY AND GEOSCIENCE. The behavior of mineral crystal structures under high-pressure is the key to understanding the deep Earth physics, and the Balić-Žunić group e.g. has discovered a new type of reversible high-pressure phase transition.^{79,80} Solid solutions are frequent in rock forming minerals, and changes in temperature and pressure can lead to breakdown of ideal solid solutions and development of microscale exsolutions. Synchrotron single crystal X-ray diffraction can resolve the structures of such intergrowths and be used to study micron-sized crystals of new minerals.⁸¹ This could bring a breakthrough in Volcanology where studies of microcrystals in lavas and sublimates from volcanic gases are key for understanding the geological processes.

A.2 Supporting information and illustrations

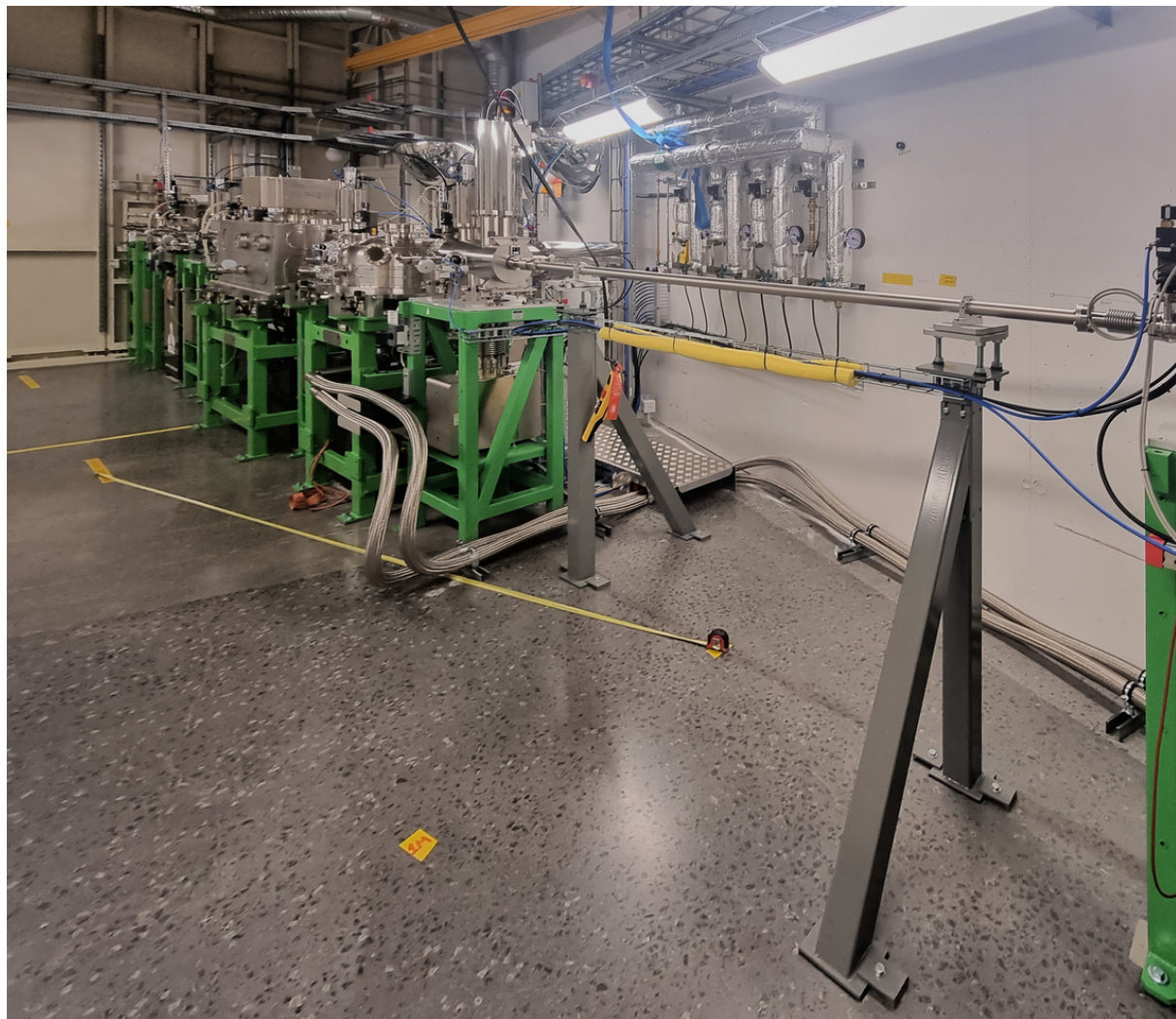


Figure 29: Photo of the optical hutch components (DanMAX). The yellow marks on the floor outline the path for the SINCRYs sidebranch. See also fig. 31 for additional CAD renders.

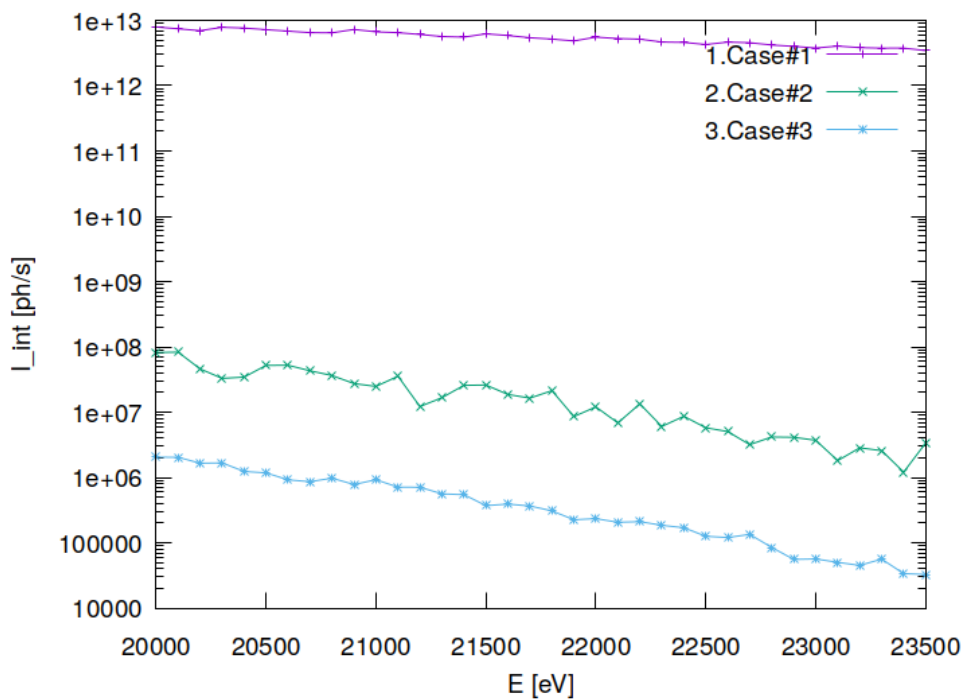


Figure 30: Photon flux in beam cross section of optical element #09 (sample). Case #1 represents the useful signal from the undulator's 9th harmonic. Case #2 and #3 are the higher harmonic contaminations with perfect alignment and with a relative misalignment by one microradian respectively. The photon energy in the abscissa of the higher harmonic curve has been divided by three to match that of the useful signal from the 9th undulator harmonic.

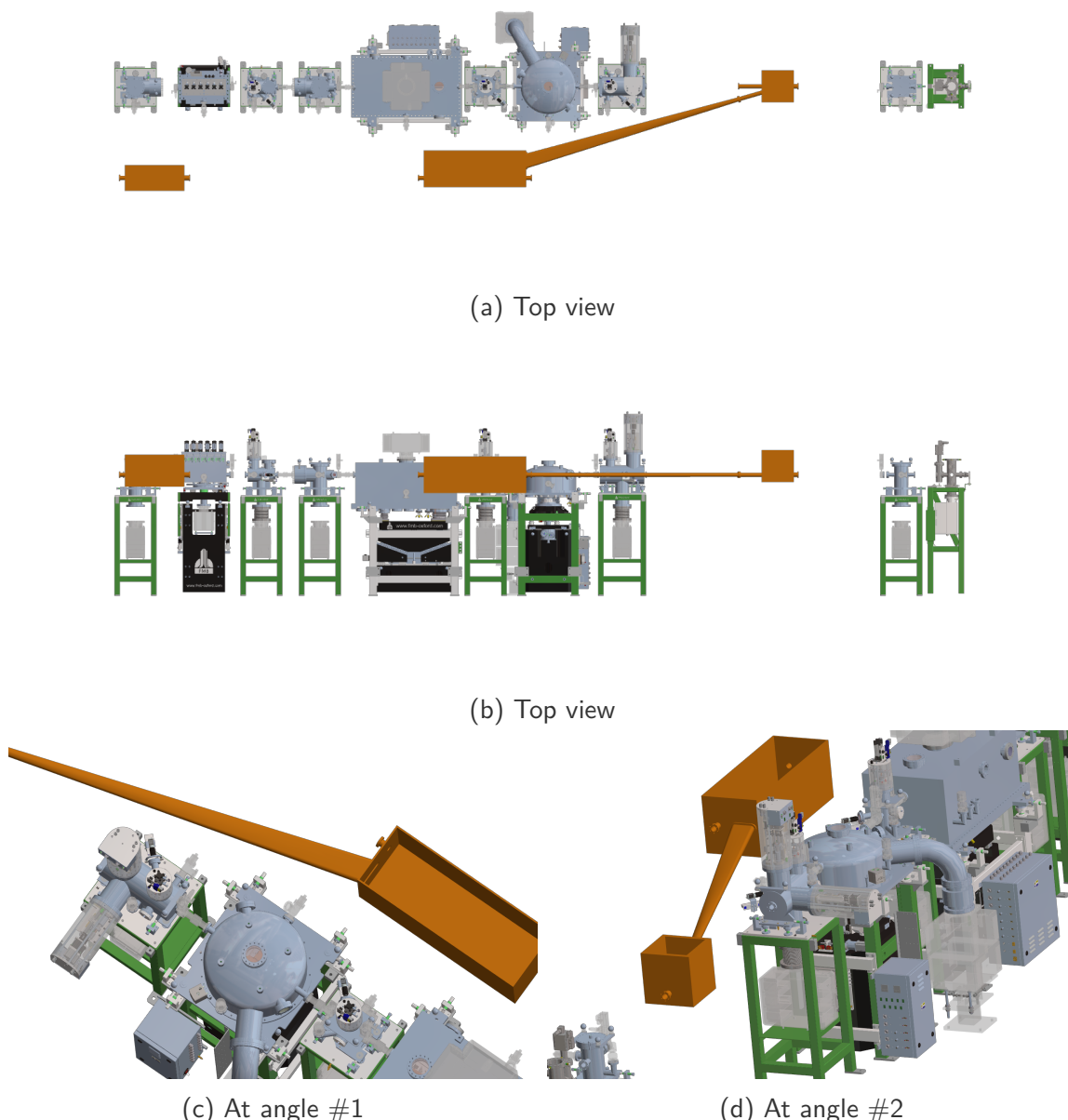


Figure 31: CAD renders of CM1, transfer pipe, CM2 and CRL box for SINCRYS in orange. Both branches end before the Beam safety shutters (not shown). The CM1 position is chosen to provide unhindered access for the DanMAX vacuum and LN2 ports, and CM2 follows. The sketched vacuum chamber walls have a minimum clearance of 10 mm to the beam.

A.3 List of Abbreviations

ANL	Argonne National Laboratory
APS	Advanced Photon Source
BCU	Beam conditioning unit
BS	Beamsplitter
BSS	Beam safety shutter
CAD	Computer aided design
C*	Diamond crystal
CF	ConFlat
CM1	Crystal monochromator 1
CM2	Crystal monochromator 2
CRL	Compound refractive lens
CVD	Chemical vapour deposition
DIAD	Dual Imaging And Diffraction
DW	Darwin width
EH	Experimental hutch
ESRF	European Synchrotron Radiation Facility
FE	Front end
FEA	Finite element analysis
FWHM	Full width half maximum
hDCM	horizontal double crystal monochromator
HERDi	High Enough Resolution Diffractometer
HPC	Hybrid photon-counting
HPF	High pass filter
HPHT	High-pressure high-temperature
HV	High vacuum
ID	Insertion device
IVU	In-vacuum undulator
LN2	Liquid nitrogen
MASH	Macros for the Automation of Shadow
NIST	National Institute of Standards and Technology
NNF	Novo Nordisk Fonden
NUFI	Nationalt Udvalg for Forskningsinfrastruktur
OH	Optics hutch
MX	macro-molecular crystallography
PAD	Pixel array detector
PLC	Programmable logic controller
POE	Power over ethernet
PSS	Personnel safety system
PXRD	Powder X-ray diffraction
SCS	Scandinavian Crystallography Service
SCXRD	Single-crystal X-ray diffraction
SOC	Sphere of confusion
UHV	Ultrahigh vacuum

A.4 Review report

The external reviewers submitted a report that details the outcome of the review that was held in April, 2023. The report is downloadable as a separate file from here: https://github.com/SinCrys/tech_report.

B Appendix B

B.1 MASH report

The full report on the ray-tracing simulations and finite element analysis is downloadable as separate file from here: https://github.com/SinCrys/tech_report.